Geochemical Perspectives Letters

Ocean mixing timescale through time and implications for the origin of iron formations

C.X. Liu[1*], A. Capirala[2], S.L. Olson[2], M.F. Jansen[3], N. Dauphas[1]

OPEN ACCESS

https://doi.org/10.7185/geochemlet.2433

Abstract

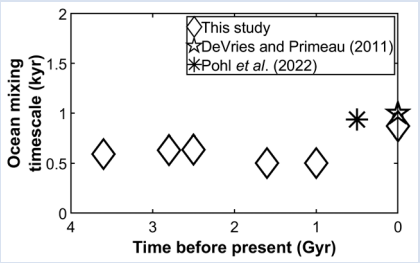

Our study examines whether the ocean mixing timescale has remained constant throughout Earth's history. If varied, it could have affected the distribution of geochemical tracers in ancient seawater, complicating interpretations of sedimentary archives. For example, the modern ocean mixing timescale is similar to the neodymium (Nd) residence time, allowing distinct Nd isotopic compositions (ε_{Nd}) to coexist in different oceanic basins. However, it is unknown whether the Archean ocean was more or less isotopically heterogeneous, and how this was recorded by banded iron formations (BIFs). We use an Earth system model to investigate the sensitivity of ocean mixing dynamics to variations in day length, surface pressure, continental configuration, and tidal dissipation. Our experiments indicate that the ocean mixing timescale fluctuated between a few hundred and a couple of thousand years since the Archean. Coupling our mixing model with a Nd cycling model in the Archean ocean, our simulations suggest that hydrothermal fluids could have mixed with other water masses carrying Nd from sediments and rivers before reaching the continental shelf. The large range of ε_{Nd} in some BIFs might therefore reflect the weathering of exposed juvenile and ancient igneous rocks, challenging prevailing views on the hydrothermal source of iron in BIFs.

Received 12 June 2023 | Accepted 5 July 2024 | Published 30 August 2024

Introduction

Ocean mixing is a key process in marine biogeochemistry, as it shapes the distribution of nutrients essential to life in the surface ocean (Meyer *et al.*, 2016) and influences the distribution of geochemical tracers in seafloor sediments that are commonly used to reconstruct ancient surface conditions (Algeo and Lyons, 2006). The overall ocean mixing timescale reflects the integrated effects of both vertical and horizontal mixing processes, and the present day ocean mixing timescale is about 1 kyr (Broecker and Peng, 1982; Matsumoto, 2007). Consequently, geochemical species with residence times that are much longer than 1 kyr are generally well mixed in seawater and can thus be considered as reliable tracers of global conditions. Changes in the abundance and/or isotopic composition of these species in marine sedimentary records are often interpreted as reflecting a different balance of sources and sinks resulting from environmental changes. Other species with oceanic residence times on the order of 1 kyr or less such as neodymium (Nd), have heterogeneous isotopic compositions in modern seawater that can be used to trace mixing between different ocean basins. A very different dynamic was advocated for the Nd cycle in the Archean, with important implications for our understanding of Superior-type BIFs deposited on passive continental margins far from volcanic sources (Gross, 1972). Early studies made the case that iron in those BIFs could have come from continental weathering (James, 1954) but the present preferred hypothesis is that fluids from deep sea hydrothermal vents enriched deep ocean waters in iron, which were upwelled to continental margins where their oxidation led to BIF deposition (Derry and Jacobsen, 1988). An important argument for a hydrothermal origin of iron in Archean BIFs is the finding of positive ε_{Nd} signatures in some. We however now understand that much of the flux of Nd in the modern oceans comes from benthic sediments (95 % of all sources) (Du *et al.*, 2020), begging the question of whether ocean mixing would have overprinted the hydrothermal signature during transit to the continental shelf.

In interpreting the chemical and isotopic compositions of sedimentary archives, it is widely assumed that the ocean mixing timescale has been similar throughout Earth's history. However, the drivers for ocean mixing like winds, tides, or density differences, are influenced by factors like day length, surface pressure, and continental configuration that have changed through Earth's history. For example, ocean mixing might have slowed due to shorter Archean day length (Bartlett and Stevenson, 2016) by altering wind driven ocean circulation (Olson *et al.*, 2020), or due to less land exposure on early Earth (Bindeman *et al.*, 2018). On the other hand, stronger tides would have strengthened mixing (Crawford *et al.*, 2022). No previous study has provided a robust quantification of the Precambrian ocean mixing timescale. Lowe (1994) hypothesised that in the Archean, high surface temperatures might have prevented the formation of marine shelf ice, potentially slowing ocean mixing timescales

1. Origins Laboratory, Department of the Geophysical Sciences and Enrico Fermi Institute, The University of Chicago, Chicago, Illinois 60637, U.S.A.
2. Department of Earth, Atmospheric, and Planetary Science, Purdue University, West Lafayette, Indiana 47907, U.S.A.
3. Department of the Geophysical Sciences, The University of Chicago, Chicago, Illinois 60637, U.S.A.
* Corresponding author (e-mail: xliu98@uchicago.edu)

to hundreds of thousands, or even millions of years. Chen *et al.* (2021) however countered that deep ocean mixing is primarily constrained by the kinetic energy input from winds and tides, and the ocean mixing timescale likely remained within a factor of 10 of the present day value. Previous modelling studies that have explored ocean mixing under conditions unlike present day Earth have focused either on Phanerozoic Earth (Pohl *et al.*, 2022) or exoplanets (Olson *et al.*, 2020), leaving a significant gap in our understanding of ocean mixing in the Precambrian era.

We use here an Earth system model called cGENIE to simulate the sensitivity of ocean mixing to day length, surface pressure, continental configuration, and tidal dissipation, first individually and then in combination. We then apply our results to explore the dynamics of Nd cycling in Archean oceans and to test the idea that Fe in BIFs was sourced from deep sea hydrothermal vents.

Methods

cGENIE includes a 3-D frictional geostrophic ocean circulation model (GOLDSTEIN) with dynamic sea ice coupled to a 2-D energy-moisture balance model of the atmosphere (EMBM; Edwards and Marsh, 2005). The ocean and the atmosphere are divided into a 36×36 equal-area latitude-longitude grid, and the ocean includes 16 depth layers. The EMBM exchanges heat and meteoric water with the underlying ocean, but does not predict planetary albedo or wind fields, which need to be prescribed in cGENIE. To generate these fields, we perform simulations using the ExoPlaSim atmospheric GCM with T21 resolution (64×32 grid; Paradise *et al.*, 2022). The decennially averaged surface wind and planetary albedo fields from ExoPlaSim are converted to cGENIE's 36×36 grid using modifications made to the 'muffingen' software and become input files for cGENIE boundary conditions.

We consider four factors that affect ocean mixing: day length, surface pressure, tidal dissipation, and continental configuration. Detailed descriptions of the corresponding code modifications and parameterisations are available in the Supplementary Information. We first carry out a series of sensitivity experiments in which we vary each of the four factors individually over a range of values or scenarios plausible for Precambrian Earth to isolate the effects of each on ocean mixing.

We then assess how day length, surface pressure, continental configuration and tidal dissipation may have jointly influenced mixing of Earth's oceans through five Precambrian eras: Paleoarchean (3.6–3.2 Ga), Neoarchean (2.8–2.5 Ga), Paleoproterozoic (2.5–1.6 Ga), Mesoproterozoic (1.6–1.0 Ga), and Neoproterozoic (1.0–0.6 Ga). Table 1 shows the parameter values adopted for each period. Day length is relatively well constrained for the Precambrian Earth, so we assign the average value from Bartlett and Stevenson (2016) to each period. Surface pressures on Archean Earth depend on nitrogen degassing and recycling between mantle and atmosphere. We test atmospheric pressures of 0.5 to 2 bar for the Archean and 1 bar for the Proterozoic (Olson *et al.*, 2018). Continental configurations in deep time are highly uncertain, so we test four configuration end members: aquaplanet, low latitude supercontinent, high latitude supercontinents, and the supercontinent Pangaea (Fig. S-7). We estimate the wind driven dissipation rate specific for each experiment from the wind speeds in the ExoPlaSim simulations (Eq. S-3) and combine it with tidal dissipation rates for the corresponding period from Webb (1982) to come up with a diapycnal diffusivity profile for each

Table 1 Model setup of historical experiments. AP: aquaplanet; LS: low latitude supercontinent; HS: high latitude supercontinents.

Period	Day length	Surface pressure	Continentality	Diapycnal diffusivity parameter
Paleoarchean (3.6–3.2 Ga)	15 hr	0.5 bar	AP	$5.6 \times 10^{-5}\ m^2\ s^{-1}$
			LS	$5.4 \times 10^{-5}\ m^2\ s^{-1}$
			HS	$5.6 \times 10^{-5}\ m^2\ s^{-1}$
		1.0 bar	AP	$5.9 \times 10^{-5}\ m^2\ s^{-1}$
			LS	$5.6 \times 10^{-5}\ m^2\ s^{-1}$
			HS	$5.8 \times 10^{-5}\ m^2\ s^{-1}$
		2.0 bar	AP	$6.1 \times 10^{-5}\ m^2\ s^{-1}$
			LS	$5.8 \times 10^{-5}\ m^2\ s^{-1}$
			HS	$6.1 \times 10^{-5}\ m^2\ s^{-1}$
Neoarchean (2.8–2.5 Ga)	18 hr	0.5 bar	AP	$4.2 \times 10^{-5}\ m^2\ s^{-1}$
			LS	$4.0 \times 10^{-5}\ m^2\ s^{-1}$
			HS	$4.1 \times 10^{-5}\ m^2\ s^{-1}$
		1.0 bar	AP	$4.4 \times 10^{-5}\ m^2\ s^{-1}$
			LS	$4.1 \times 10^{-5}\ m^2\ s^{-1}$
			HS	$4.4 \times 10^{-5}\ m^2\ s^{-1}$
Paleoproterozoic (2.5–1.6 Ga)	18 hr	1.0 bar	LS	$3.6 \times 10^{-5}\ m^2\ s^{-1}$
			HS	$3.8 \times 10^{-5}\ m^2\ s^{-1}$
			Pangaea	$3.7 \times 10^{-5}\ m^2\ s^{-1}$
Mesoproterozoic (1.6–1.0 Ga)	22.5 hr	1.0 bar	LS	$1.9 \times 10^{-5}\ m^2\ s^{-1}$
			HS	$2.2 \times 10^{-5}\ m^2\ s^{-1}$
			Pangaea	$2.1 \times 10^{-5}\ m^2\ s^{-1}$
Neoproterozoic (1.0–0.6 Ga)	22.5 hr	1.0 bar	LS	$1.9 \times 10^{-5}\ m^2\ s^{-1}$
			HS	$2.2 \times 10^{-5}\ m^2\ s^{-1}$
			Pangaea	$2.1 \times 10^{-5}\ m^2\ s^{-1}$

experiment. We use pre-industrial solar forcing, atmospheric chemistry, and geothermal heat flux across our experiments to isolate the effects of Earth's geophysical and planetary evolution on ocean mixing timescale, except in experiments with non-present day-level surface pressure where we remove ozone (Supplementary Information). To provide a baseline for each of the two scenarios (with and without ozone), we model the present day ocean mixing with (present day baseline) and without (ozone-less baseline) ozone.

We run each of our experiments for 10,000 model years to achieve steady state and capture long term mean ocean circulation. Six historical experiments reach a snowball state due to global cooling induced by lowered surface pressures and increased rotation rates. For the remaining experiments, we take the mean benthic (>2 km deep ocean floor) and maximum global ventilation ages as diagnostics for the ocean mixing timescale. Ventilation age is a measure of vertical mixing, where age is reset when a water parcel is at the top of the water column, not when different oceanic basins are homogenised (Ridgwell, 2017). In practice, however, this is also an approximate measure of lateral mixing in the deep ocean, since the ages of the oldest water masses are limited by lateral transport from the regions of deep water formation to the rest of global deep ocean.

Building upon our understanding of Precambrian ocean mixing, we explore the potential of Nd isotopes as a geochemical tracer of water mass provenance and source of rare earth elements (REEs) and iron in Archean oceans. Our modelling of the modern Nd cycle shows that we can reproduce well the basinal heterogeneity of ε_{Nd} in the modern ocean (Fig. S-3). To model the Archean oceanic Nd cycle, we estimate Nd input fluxes from rivers, aeolian dust and hydrothermal vents using similar scaling arguments as those used for Fe by Dauphas *et al.* (2024). The Nd flux from benthic sediments and isotopic heterogeneity of various sources in the Archean are uncertain. To address this, we conducted four simulations (Table S-1), where mass balance is always adjusted to reproduce the average ε_{Nd} value of Superior-type BIFs (Fig. 3a) and the residence time is set to 643 yr (Supplementary Information):

Scenario 1. Each source has a homogeneous isotopic composition, and the benthic sediment source represents 95 % of the total Nd input flux.

Scenario 2. Same as Scenario 1 but the benthic source is reduced as it is only 95 % of the flux comprising benthic, riverine and aeolian sources.

Scenario 3. Same as Scenario 1 but the benthic source is isotopically heterogeneous depending on the distance from continental and hydrothermal sources.

Scenario 4. Same as Scenario 2 but we allow for a hemispheric dichotomy in the ε_{Nd} values of benthic and continental sources.

Results and Discussion

Variation in ocean mixing timescale through Earth's history. In our modelled present day oceans, the mean benthic ventilation age is 0.79 kyr and the maximum global ventilation age is 1.3 kyr (Figs. 1, S-4), slightly shorter than the data constrained model estimates of present day ventilation ages from DeVries and Primeau (2011). Nonetheless, climatology fields from our model resemble observed pre-industrial distributions (Figs. S-5, S-6), supporting our model's accuracy in simulating the ocean mixing timescale through time.

Day length and ocean mixing timescale are negatively correlated. Increasing day length from 15 to 24 hr decreases mean benthic ventilation age by 0.32 kyr and maximum global ventilation age by 0.47 kyr (Fig. 1a). This inverse relationship between ocean mixing timescale and day length is qualitatively consistent with the expectation that wind driven Ekman transport strengthens with longer day length (Olson *et al.*, 2020). Ekman transport ($m^2\ s^{-1}$) is calculated as the horizontal velocity integrated in the vertical direction, $V = \tau/(2\rho\Omega \sin\varphi)$, where τ is wind stress (Pa), ρ is seawater density ($kg\ m^{-3}$), Ω is planet's rotation rate ($rad\ s^{-1}$) and φ is latitude (degrees). When day length increases (equivalently, rotation rate Ω decreases), Ekman transport induced by a given wind stress increases, causing the ocean's overturning circulation to strengthen (Nikurashin and Vallis, 2012).

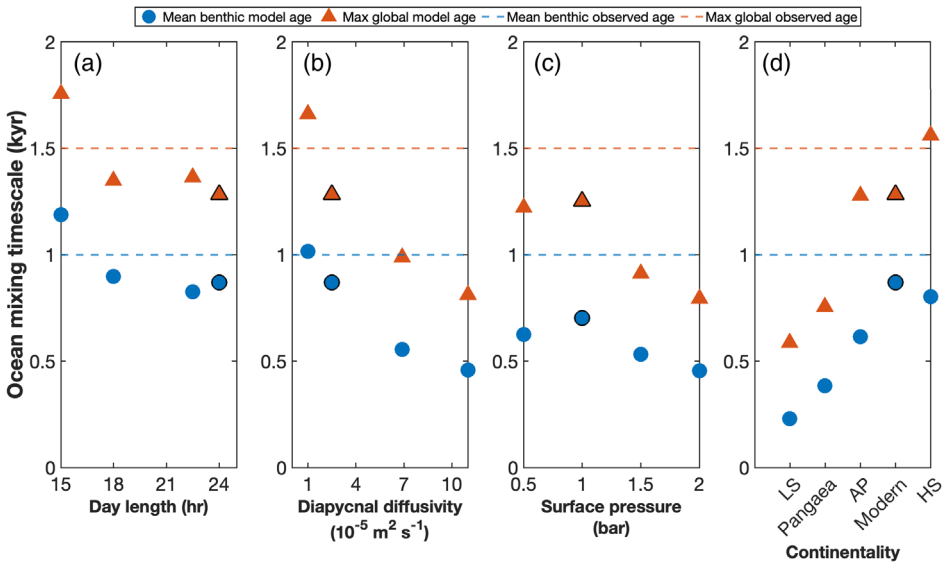

Figure 1 Sensitivity of the ocean mixing timescale to Earth's day length, tidal dissipation, surface pressure, and continental configuration. Dashed lines are data constrained model estimates of present day ventilation ages from DeVries and Primeau (2011). Symbols with black outline indicate present day baseline ages **in (a), (b), (d)** and ozone-less baseline ages in **(c)**. AP: aquaplanet; LS: low latitude supercontinent; HS: high latitude supercontinents.

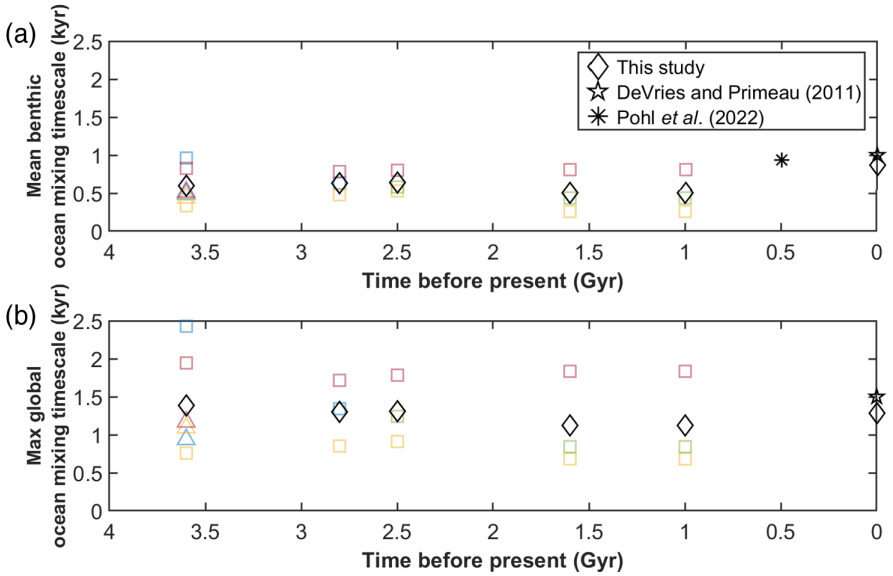

Figure 2 Variation in mean benthic **(a)** and maximum global **(b)** ocean mixing timescales through time. Squares and triangles correspond to historical experiments with surface pressure of 1 bar and 2 bar, respectively. Continental configuration is represented by blue (aquaplanet), yellow (low latitude supercontinent), red (high latitude supercontinents), and green (Pangaea) symbols. The black diamond at 0 Gyr is our present day baseline experiment, while black diamonds for the historical periods give the mean values of all experiments in the respective period. The asterisk at 0.5 Gyr is modelled Phanerozoic mean benthic ventilation age from Pohl *et al.* (2022), and the pentagrams at 0 Gyr are data constrained model estimates of present day ventilation ages from DeVries and Primeau (2011).

Diapycnal diffusivity (κ) and ocean mixing timescale are also negatively correlated. A ten fold increase in κ reduces mean benthic ventilation age by 0.56 kyr and maximum global ventilation age by 0.85 kyr (Fig. 1b). Diapycnal diffusivity affects the ocean mixing timescale both directly *via* diffusive transport of tracers and indirectly *via* the global overturning circulation (Nikurashin and Vallis, 2012).

Atmospheric surface pressure and ocean mixing timescale are negatively correlated beyond 1 bar. Increasing surface pressure from 1 to 2 bar decreases the mean benthic ventilation age by 0.25 kyr and the maximum global ventilation age by 0.46 kyr (Fig. 1c). Surface pressure affects ocean mixing *via* changes in the wind stress $\boldsymbol{\tau} = c_a \rho_a |\boldsymbol{u}| \boldsymbol{u}$, where $\boldsymbol{u}$ is wind speed and $|\boldsymbol{u}|$ is its magnitude (m s^{-1}), c_a is a dimensionless drag coefficient, and ρ_a is air density (kg m^{-3}). Increasing surface pressure increases air density more significantly than it decreases wind speed due to friction, thereby increasing wind stress (Fig. S-13), which in turn enhances ocean mixing. A deviation from this trend is found at surface pressure lower than 1 bar, possibly resulting from increased sea ice cover at low surface pressure (Olson *et al.*, 2020).

Continentality configurations with more land mass present in the high latitudes than the low latitudes have longer ocean mixing timescales, with the mean benthic ventilation age varying between 0.23 and 0.80 kyr and the maximum global ventilation age between 0.59 and 1.6 kyr (Fig. 1d). The reasons for this behaviour are not entirely clear, although multiple mechanisms may contribute. Low latitude landmasses tend to reduce oceanic meridional heat transport out of the tropics (Enderton and Marshall, 2009), resulting in a larger equator-to-pole temperature difference that may strengthen deep ocean overturning circulation. Moreover, in our simulations, we find deep water formation at both poles (with upwelling in the low latitudes) in the case of a low latitude supercontinent, while the aquaplanet and high latitude supercontinent setups exhibit deep water formation in only one hemisphere (Fig. S-8). The latter result, however, may depend on details of the model configuration (Enderton and Marshall, 2009).

Our sensitivity tests highlight the fact that multiple factors could have influenced ocean mixing through Earth's history, several of which act in opposing directions. Consequently, we find that the variations in ocean mixing timescale are relatively minor in our experiments aimed at simulating different Precambrian eras (Fig. 2). The mean benthic ventilation age varies from 0.26 to 0.96 kyr, and the maximum global ventilation age varies from 0.68 to 2.4 kyr. We therefore conclude that the ocean mixing timescale remained broadly like the present day value, varying between a few hundred and a couple of thousand years through the Precambrian (Figs. S-9 to S-12).

Neodymium isotopes as tracers of water mass provenance and REE (and Fe) sources in Superior-type banded iron formations. In Figure 3b, the calculated seawater ε_{Nd} at ocean depths relevant to BIF deposition exhibits the following ranges respectively: +0.56 to +0.69 (Scenario 1), +0.39 to +0.87 (Scenario 2), +0.30 to +1.0 (Scenario 3), and −1.2 to +2.3 (Scenario 4). Archean Superior-type BIFs (Fig. 3a) have ε_{Nd} ranging from −3.5 to +5.3 with an interquartile range of −0.6 to +2.1. Scenarios 1, 2 and 3 cannot explain this range. In Scenario 4, which involves a smaller benthic flux and a drastic heterogeneity in the isotopic compositions of continental and benthic sources (reflecting, for example, contributions from juvenile and ancient crust), we can reproduce that range.

All our flux estimates give the benthic sediment flux as the dominant Nd source in the Archean oceans, representing 79 % to 95 % of the total. Our Nd isotope modelling results show that under those circumstances, it is difficult for the hydrothermal ε_{Nd} signature to be expressed in BIFs deposited in continental shelf environments. Instead, the source of positive ε_{Nd} in BIFs could be juvenile emerged crust, most likely derived secondarily from benthic sediments, as documented in modern porewater and authigenic ε_{Nd} in the North Pacific (Du *et al.*, 2016). Kamber (2010) argued for the weathering of juvenile emerged lands as the source of positive ε_{Nd} in BIFs, but there is no robust evidence for a large dominance of mafic rocks at that time. Examination of detrital sediments shows that

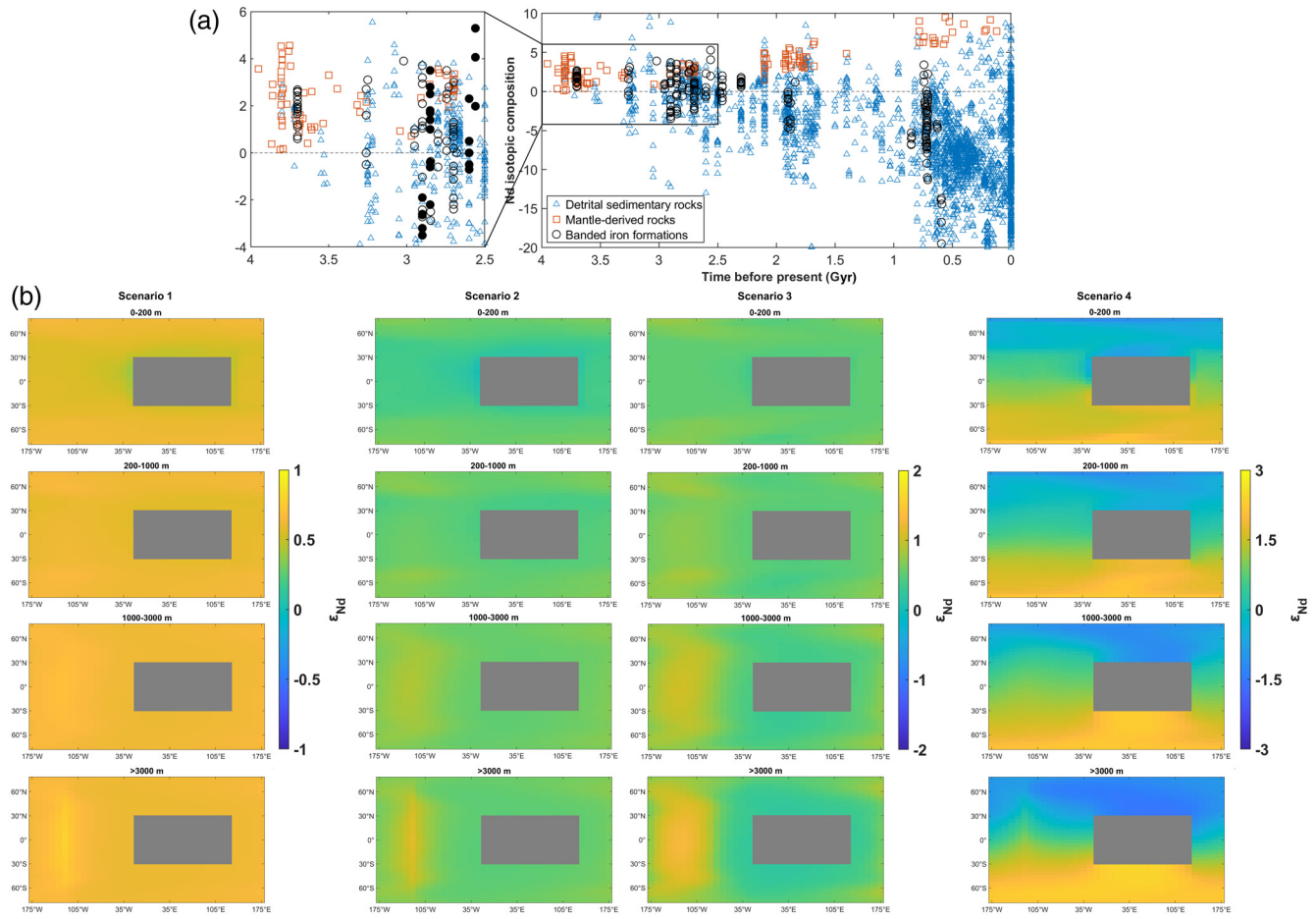

Figure 3 **(a)** Temporal evolution of ε_{Nd} of Precambrian BIFs (black circles; Hu *et al.*, 2020; Haugaard *et al.*, 2016), depleted mantle-derived basalts (orange squares; Vervoort and Blichert-Toft, 1999) and detrital sedimentary rocks (blue triangles; Garçon, 2021). Archean Superior-type BIFs are represented by black filled circles in the zoom-in view. **(b)** Modelled seawater ε_{Nd} averaged over various column depths in the Archean ocean with mean benthic ventilation age of 0.33 kyr. The four scenarios are detailed in the main text and Supplementary Information.

young continental crust comprising both mafic and felsic rocks extracted from depleted sources existed at that time (Garçon, 2021), which through weathering could have supplied highly heterogeneous ε_{Nd} to the oceans. The role of hydrothermal fluids in BIF deposition could have therefore been less significant than previously thought, with continental weathering being the main source of Fe and Nd to the oceans.

Conclusions and Implications

Our study provides the first quantitative evidence that despite changes in Earth's day length, surface pressure, continentality, and tidal dissipation, the ocean mixing timescale has remained relatively constant through geological eons, likely varying between a few hundred and a couple of thousand years since the Archean. Coupling this model of physical mixing with a model of Nd cycling in Archean oceans challenges the prevailing view that Fe and Nd in Superior-type BIFs come from hydrothermal sources. Instead, it suggests that Fe and Nd might have been derived from heterogeneous continental crust made of ancient and juvenile igneous rocks.

Acknowledgements

This work was supported by grants 80NSSC20K1409 (NASA-HW) to SO, MJ, and ND, 80NSSC23K1022 (NASA-LARS), 80NSSC21K0380 (NASA-EW), 80NSSC23K1163 (NASA-MMX), EAR-2001098 (NSF-CSEDI), and DE-SC0022451 (DOE) to ND.

Editor: Claudine Stirling

Author Contributions

CL, ND, SO, and MJ conceived the study. CL ran the cGENIE experiments with input from SO and MJ. AC ran the ExoPlaSim experiments and coded wind and albedo re-gridding. CL developed ε_{ed} modelling with input from ND, SO and MJ. CL and ND wrote the first draft of the manuscript, which was subsequently edited by all the co-authors.

Additional Information

Supplementary Information accompanies this letter at https://www.geochemicalperspectivesletters.org/article2433.

Cite this letter as: Liu, C.X., Capirala, A., Olson, S.L., Jansen, M.F., Dauphas, N. (2024) Ocean mixing timescale through time and implications for the origin of iron formations. *Geochem. Persp. Let.* 31, 54–59. https://doi.org/10.7185/geochemlet.2433

References

Algeo, T.J., Lyons, T.W. (2006) Mo–total organic carbon covariation in present-day anoxic marine environments: Implications for analysis of paleoredox and paleohydrographic conditions. *Paleoceanography* 21, PA1016. https://doi.org/10.1029/2004PA001112

Bartlett, B.C., Stevenson, D.J. (2016) Analysis of a Precambrian resonance-stabilized day length. *Geophysical Research Letters* 43, 5716–5724. https://doi.org/10.1002/2016GL068912

Bindeman, I.N., Zakharov, D.O., Palandri, J., Greber, N.D., Dauphas, N., *et al.* (2018) Rapid emergence of subaerial landmasses and onset of a modern hydrologic cycle 2.5 billion years ago. *Nature* 557, 545–548. https://doi.org/10.1038/s41586-018-0131-1

Broecker, W.S., Peng, T.H. (1982) *Tracers in the Sea* (vol. 690). Palisades, New York: Lamont-Doherty Geological Observatory, Columbia University. https://doi.org/10.1017/S0033822200005221

Chen, X., Tissot, F.L.H., Jansen, M.F., Bekker, A., Liu, C.X., Nie, N.X., Halverson, G.P., Veizer, J., Dauphas, N. (2021) The uranium isotopic record of shales and carbonates through geologic time. *Geochimica et Cosmochimica Acta* 300, 164–191. https://doi.org/10.1016/j.gca.2021.01.040

Crawford, E.B., Arbic, B.K., Sheldon, N.D., Ansong, J.K., Timko, P.G. (2022) Investigating the behavior of mid-Archean tides and potential implications for biogeochemical cycling. *Precambrian Research* 380, 106799. https://doi.org/10.1016/j.precamres.2022.106799

Dauphas, N., Heard, A.W., Rego, E.S., Rouxel, O., Marin-Carbonne, J., Pasquier, V., Bekker, A., Rowley, D.B., (2024) Past and present dynamics of the iron biogeochemical cycle. *Reference Module in Earth Systems and Environmental Sciences*. https://doi.org/10.1016/B978-0-323-99762-1.00059-0

Derry, L.A., Jacobsen, S.B. (1988) The Nd and Sr isotopic evolution of Proterozoic seawater. *Geophysical Research Letters* 15, 397–400. https://doi.org/10.1029/GL015i004p00397

DeVries, T., Primeau, F. (2011) Dynamically and observationally constrained estimates of water-mass distributions and ages in the global ocean. *Journal of Physical Oceanography* 41, 2381–2401. https://doi.org/10.1175/JPO-D-10-05011.1

Du, J., Haley, B.A., Mix, A.C. (2016) Neodymium isotopes in authigenic phases, bottom waters and detrital sediments in the Gulf of Alaska and their implications for paleo-circulation reconstruction. *Geochimica et Cosmochimica Acta* 193, 14–35. https://doi.org/10.1016/j.gca.2016.08.005

Du, J., Haley, B.A., Mix, A.C. (2020) Evolution of the Global Overturning Circulation since the Last Glacial Maximum based on marine authigenic neodymium isotopes. *Quaternary Science Reviews* 241, 106396. https://doi.org/10.1016/j.quascirev.2020.106396

Edwards, N.R., Marsh, R. (2005) Uncertainties due to transport-parameter sensitivity in an efficient 3-D ocean-climate model. *Climate Dynamics* 24, 415–433. https://doi.org/10.1007/s00382-004-0508-8

Enderton, D., Marshall, J. (2009) Explorations of atmosphere–ocean–ice climates on an aquaplanet and their meridional energy transports. *Journal of the Atmospheric Sciences* 66, 1593–1611. https://doi.org/10.1175/2008JAS2680.1

Garçon, M. (2021) Episodic growth of felsic continents in the past 3.7 Ga. *Science Advances* 7, eabj1807. https://doi.org/10.1126/sciadv.abj1807

Gross, G.A. (1972) Primary features in cherty iron-formations. *Sedimentary Geology* 7, 241–261. https://doi.org/10.1016/0037-0738(72)90024-3

Haugaard, R., Ootes, L., Creaser, R.A., Konhauser, K.O. (2016) The nature of Mesoarchaean seawater and continental weathering in 2.85 Ga banded iron formation, Slave craton, NW Canada. *Geochimica et Cosmochimica Acta* 194, 34–56. https://doi.org/10.1016/j.gca.2016.08.020

Hu, J., Wang, H., Zhang, L. (2020) A rare earth element and Nd isotopic investigation into the provenance and deposition of the Dahongliutan banded iron formation and associated carbonates, NW China: Implications on Neoproterozoic seawater compositions. *Precambrian Research* 342, 105685. https://doi.org/10.1016/j.precamres.2020.105685

James, H.L. (1954) Sedimentary facies of iron-formation. *Economic Geology* 49, 235–293. https://doi.org/10.2113/gsecongeo.49.3.235

Kamber, B.S. (2010) Archean mafic–ultramafic volcanic landmasses and their effect on ocean–atmosphere chemistry. *Chemical Geology* 274, 19–28. https://doi.org/10.1016/j.chemgeo.2010.03.009

Lowe, D.R. (1994) Early environments: constraints and opportunities for early evolution. *Early life on Earth*, 25–35.

Matsumoto, K. (2007) Radiocarbon-based circulation age of the world oceans. *Journal of Geophysical Research: Oceans* 112, C09004. https://doi.org/10.1029/2007JC004095

Meyer, K.M., Ridgwell, A., Payne, J.L. (2016) The influence of the biological pump on ocean chemistry: implications for long-term trends in marine redox chemistry, the global carbon cycle, and marine animal ecosystems. *Geobiology* 14, 207–219. https://doi.org/10.1111/GBI.12176

Nikurashin, M., Vallis, G. (2012) A theory of the interhemispheric meridional overturning circulation and associated stratification. *Journal of Physical Oceanography* 42, 1652–1667. https://doi.org/10.1175/JPO-D-11-0189.1

Olson, S.L., Schwieterman, E.W., Reinhard, C.T., Lyons, T.W. (2018) Earth: Atmospheric Evolution of a Habitable Planet. In: Deeg, H., Belmonte, J. (Eds.) *Handbook of Exoplanets*. Springer, Cham. https://doi.org/10.1007/978-3-319-55333-7_189

Olson, S.L., Jansen, M., Abbot, D.S. (2020) Oceanographic Considerations for Exoplanet Life Detection. *The Astrophysical Journal* 895, 19. https://doi.org/10.3847/1538-4357/ab88c9

Paradise, A., Macdonald, E., Menou, K., Lee, C., Fan, B.L. (2022) ExoPlaSim: Extending the Planet Simulator for exoplanets. *Monthly Notices of the Royal Astronomical Society* 511, 3272–3303. https://doi.org/10.1093/mnras/stac172

Pohl, A., Ridgwell, A., Stockey, R.G., Thomazo, C., Keane, A., Vennin, E., Scotese, C.R. (2022) Continental configuration controls ocean oxygenation during the Phanerozoic. *Nature* 608, 523–527. https://doi.org/10.1038/s41586-022-05018-z

Ridgwell, A. (2017) The Bumper Book of muffins (The cGENIE.muffin user-manual and introduction to Earth system modelling). https://www.seao2.info/cgenie/docs/muffin.pdf

Vervoort, J.D., Blichert-Toft, J. (1999) Evolution of the depleted mantle: Hf isotope evidence from juvenile rocks through time. *Geochimica et Cosmochimica Acta* 63, 533–556. https://doi.org/10.1016/S0016-7037(98)00274-9

Webb, D.J. (1982) Tides and the evolution of the Earth-Moon system. *Geophysical Journal International* 70, 261–271. https://academic.oup.com/gji/article-abstract/70/1/261/708791

Geochemical Perspectives Letters

Ocean mixing timescale through time and implications for the origin of iron formations

C.X. Liu, A. Capirala, S.L. Olson, M.F. Jansen, N. Dauphas

Supplementary Information

The Supplementary Information includes:

- Parameterization of the effect of tidal dissipation and wind energy input on diapycnal mixing
- Modification of day length in cGENIE
- Setup of ExoPlaSim simulations and boundary conditions for cGENIE
- Setup of Nd isotope modelling in cGENIE
- Supplementary Figures S-1 to S-13
- Supplementary Table S-1
- Supplementary Information References

Parameterization of the effect of tidal dissipation and wind energy input on diapycnal mixing

GOLDSTEIN, the ocean circulation model within cGENIE, uses a stratification-dependent diapycnal mixing scheme (Oliver and Edwards, 2008):

$$\kappa(z) = \kappa_c f(z) \times (\rho_{z,lev}(z)/\rho_z(z)), \qquad \text{(Eq. S-1)}$$

where $f(z) = e^{-(2500m-z)/700m}$ is a reference vertical profile exponentially growing with depth and equal to 1 at a depth of 2500 m, $\rho_z(z)$ is the density stratification, $\rho_{z,lev}(z) = (-5.5 \times 10^{-3})e^{z/650m}\ kg\ m^{-4}$ is a reference stratification profile, and κ_c is the diffusivity at 2500 m when $\rho_z(z) = \rho_{z,lev}(z)$. κ_c is treated as an adjustable parameter and is set to $2.5 \times 10^{-5}\ m^2\ s^{-1}$ in our present-day ocean reference case. The resulting diffusivity profile is broadly consistent with observations (Fig. S-1), with values below $10^{-5}\ m^2\ s^{-1}$ in the thermocline and around $10^{-4}\ m^2\ s^{-1}$ at depth (Kunze *et al*., 2006).

For a given stratification, with its effect explicitly accounted for in Eq. S-1, diapycnal diffusivity κ is expected to be proportional to the turbulent kinetic energy dissipation rate ε in the ocean interior, which derives mainly from breaking of internal waves that are ultimately driven by lunisolar tides and surface wind stress (0.3 and 0.1 TW respectively for input rates of energy into vertical mixing below the mixed layer, Yang *et al*., 2017). We therefore expect $\kappa_c/\kappa_{c,m} = \varepsilon/\varepsilon_m = (\varepsilon_t + \varepsilon_w)/\varepsilon_m = (\varepsilon_t/\varepsilon_{t,m})(\varepsilon_{t,m}/\varepsilon_m) + (\varepsilon_w/\varepsilon_{w,m})(\varepsilon_{w,m}/\varepsilon_m)$, where the subscript m indicates present-day conditions, ε_t is the tidal energy dissipation rate, and ε_w is wind-driven turbulent dissipation rate. Waterhouse *et al.* (2014) suggest that tides contribute about 3/4 of the dissipation rate today, thus indicating that $\varepsilon_{t,m}/\varepsilon_m \approx 3/4$, while $\varepsilon_{w,m}/\varepsilon_m \approx 1/4$. We therefore have,

$$\kappa_c/\kappa_{c,m} = \frac{3}{4}(\varepsilon_t/\varepsilon_{t,m}) + \frac{1}{4}(\varepsilon_w/\varepsilon_{w,m}). \quad \text{(Eq. S-2)}$$

Lunisolar tides would have changed in the past due to the greater proximity of the Moon and different continentalities. Assuming a present-day continental configuration, Webb (1982) calculated the influence of Earth-Moon distance on tidal dissipation through time. Assuming that the fraction of tidal dissipation that contributes to deep ocean mixing stayed roughly constant through time, the results suggest that $\varepsilon_t/\varepsilon_{t,m} = 0.7, 0.7, 1.6, 1.9, 2.7$ at 1, 1.6, 2.5, 2.8 and 3.6 Ga respectively.

Davies *et al*. (2020) found that the deep ocean tidal dissipation rate could vary by about a factor of 4 depending on the continental configuration. To take the continentality effect into account, we therefore apply a factor of 0.5 to the minimum $\varepsilon_t/\varepsilon_{t,m}$ and a factor of 2 to the maximum $\varepsilon_t/\varepsilon_{t,m}$ obtained from Webb (1982), resulting in a likely range for $\varepsilon_t/\varepsilon_{t,m}$ between 0.35 and 5.4.

We estimate $\varepsilon_w/\varepsilon_{w,m}$ in our simulations by estimating the spatially integrated wind energy dissipation over the ocean surface and normalizing it with the present-day value,

$$\frac{\varepsilon_w}{\varepsilon_{w,m}} = \frac{p}{p_m}\frac{\int v^2 dA}{\int {v_m}^2 dA}, \quad \text{(Eq. S-3)}$$

where p is mean surface pressure in bar and v is surface wind speed in m/s. We calculate $\varepsilon_w/\varepsilon_{w,m}$ for three groups of sensitivity experiments: continentality, surface pressure, and day length, as well as all the historical simulations from ExoPlaSim. The minimum and maximum $\varepsilon_w/\varepsilon_{w,m}$ values across all simulations are 0.61 and 1.7, which we use as the likely range for our diffusivity sensitivity experiments.

To estimate the minimum and maximum diffusivities, we combine the minimum and maximum of $\varepsilon_t/\varepsilon_{t,m}$ and $\varepsilon_w/\varepsilon_{w,m}$ respectively, which yields $\kappa_{c,min} = 1.0 \times 10^{-5}\, m^2\, s^{-1}$ and $\kappa_{c,max} = 1.1 \times 10^{-4}\, m^2\, s^{-1}$. Including the present-day baseline case with $\kappa_c = 2.5 \times 10^{-4}\, m^2\, s^{-1}$, and an additional intermediate value with $\kappa_c = 6.9 \times 10^{-5}\, m^2\, s^{-1}$ we therefore have four experiments in our diffusivity sensitivity series: $\kappa_c = 1.0 \times 10^{-5}, 2.5 \times 10^{-5}, 6.9 \times 10^{-5}, 1.1 \times 10^{-4}\, m^2 s^{-1}$. For the historical period simulations, we take $\varepsilon_t/\varepsilon_{t,m}$ for the corresponding time period from Webb (1982) and the estimated $\varepsilon_w/\varepsilon_{w,m}$ values from Eq. S-3 specific to the respective simulation. The resulting diapycnal diffusivity values, computed using Eq. S-2, are provided in Table 1.

Modification of day length in cGENIE

Solar day length was explicitly hard-coded at its present-day value (86400 seconds/day) in the GOLDSTEIN ocean, GOLDSTEIN-SEAICE sea-ice, and EMBM atmosphere modules within the cGENIE model. In addition, present-day sidereal day length was implicitly used in deriving the scaled Coriolis coefficient $fsc = 2 \times 7.2921 \times 10^{-5} = 2 \times 2\pi/86164$. To enable simulations with day lengths (rotation rates) different from Earth's modern 24 hr day length, we introduce solar day length and sidereal day length in cGENIE as namelist parameters, following the instructions in Ridgwell (2017). The code for the version of the "muffin" release of the cGENIE Earth system model used in this paper is tagged as v0.9.50 and is assigned a DOI: 10.5281/zenodo.10798347.

cGENIE assumes a default year length of 365.25 days/year. In this paper, we modify the number of days per year such that all simulations have the same orbital period (total seconds/year).

Setup of ExoPlaSim simulations and boundary conditions for cGENIE

Atmospheric modeling in ExoPlaSim. cGENIE does not model a dynamic atmosphere and requires prescribed atmospheric and surface boundary conditions to force ocean circulation. These inputs are in the form of wind stress fields and zonally-averaged planetary albedo. The variations in wind patterns and planetary albedo are significant when varying rotation rate and surface pressure, so to account for the effect on wind-driven circulation, we first conduct equivalent simulations using ExoPlaSim v. 3.0.6 (Paradise *et al*., 2022; pypi.org/project/exoplasim/3.0.6/), a modified version of the Planet Simulator (PlaSim, Fraedrich *et al*., 2005). ExoPlaSim is a fast atmospheric GCM modified to

simulate a wider variety of non-Earth-like planets, including different rotation rates and surface pressures. We run our simulations at T21 resolution (32 latitudes by 64 longitudes), 10 atmospheric layers, and all present-day Earth-like parameters except for rotation rate, surface pressure, and land map as varied across our experiments. ExoPlaSim uses a slab ocean that lacks dynamic heat transport and simulates a mixed layer of constant depth (set in our experiments to 100 m) and constant heat capacity (set by the model to 4180 J kg^{-1} K^{-1}). A present-day Earth-like climate is also imposed for all experiments at 1 atm pressure by using modern solar flux and pre-industrial levels of pCO_2, and climate is thus only allowed to vary in response to our parameters of interest. ExoPlaSim's atmospheric composition comprises only N_2, CO_2, H_2O, and O_3, which is sufficient to produce a realistic behavior. At pressures other than 1 atm, pN_2 and pCO_2 are both multiplied to keep their relative amounts constant.

Ozone is handled differently in our experimental configurations. Due to its role in stratospheric warming, O_3 is necessary to produce modern Earth surface temperatures and reasonable extents of sea-ice in the model. However, the climate responds unrealistically to ozone present in the atmosphere at higher surface pressures. When pressures increase, a higher number of collisional interactions between molecules in the atmosphere affects the absorption and emission of infrared radiation, causing increased greenhouse warming (termed pressure broadening). This effect is parameterized in ExoPlaSim as an idealized multiplicative parameter that alters absorption by O_3, CO_2, and H_2O by adjusting the amount of effective absorber (Paradise *et al.*, 2021). Pressure broadening offsets the significant cooling effect of Rayleigh scattering that also occurs at higher pressures. At 2 atm surface pressure, we find that O_3 generates a strong warming positive feedback with water vapor when pressure broadening is applied to both absorbers, generating surface temperatures that are unrealistic for any time period in our study (mean global temperatures upwards of 60 ° C and maximum temperatures around 75-80 °C). Therefore, we enable O_3 only in simulations where the surface pressure is 1 atm. A 1 atm simulation without ozone is provided for comparison with the pressure sensitivity experiments (Fig. S-2).

Boundary conditions in cGENIE. To derive required boundary conditions for cGENIE's ocean circulation (wind fields and planetary albedo), we implement modifications to the 'muffingen' open source software version v0.9.21 (DOI: 10.5281/zenodo.10802839), which in its original state takes output files from coupled GCM experiments to create a full set of input files for running an equivalent simulation in cGENIE. Our modified scripts re-grid and convert only ExoPlaSim wind stress, velocity, and radiation outputs to input files for cGENIE's 36×36 grid. A supplementary script

converts cGENIE land-sea mask files to ExoPlaSim landmap files so that the spatial boundary conditions correctly align with the topography of the cGENIE experiment.

Wind stress fields required by cGENIE's GOLDSTEIN, GOLDSTEIN-SEAICE, and EMBM modules are in the form of x- and y- component (eastward and northward) wind stress at the u and v grid points of cGENIE's Arakawa C grid. An additional wind speed field, computed as the vector magnitude of the x- and y- wind velocity from ExoPlaSim, is used by the EMBM. Planetary albedo is calculated as the ratio between total annual incoming and outgoing shortwave radiation at the top of the atmosphere and it is regridded to a zonally averaged planetary albedo. All regridded products are generated from an average of the last 10 simulation years in ExoPlaSim to account for minor inter-annual variations in output variables or different monthly averaging at non-present-day day lengths. Finally, we adjust the wind-stress scaling parameter in the cGENIE model to achieve comparable modern global ventilation ages using ExoPlaSim wind fields. Because cGENIE by default calibrates its wind-driven circulation to the magnitude of its own internal wind field when external GCM wind fields are not applied, this adjustment is necessary to compensate for the differences in how the two models—ExoPlaSim and cGENIE—calculate and report the average magnitude of wind stress (*e.g.*, Crichton *et al.*, 2021).

Setup of Nd isotope modelling in cGENIE

To estimate the Nd-$\boldsymbol{\varepsilon}_{\mathrm{Nd}}$ budget for Archean oceans (Table S-1), we need to know the following:

1. The residence time of Nd.
2. Nd input fluxes (g/yr) of rivers ($\phi_{\mathrm{Nd,r}}$), aeolian dust ($\phi_{\mathrm{Nd,d}}$), hydrothermal fluids ($\phi_{\mathrm{Nd,h}}$) and benthic sediments ($\phi_{\mathrm{Nd,s}}$).
3. Global mean Nd isotopic compositions of seawater ($\varepsilon_{\mathrm{Nd,sw}}$), river ($\varepsilon_{\mathrm{Nd,r}}$), aeolian dust ($\varepsilon_{\mathrm{Nd,d}}$), hydrothermal fluid ($\varepsilon_{\mathrm{Nd,h}}$), and benthic sediment ($\varepsilon_{\mathrm{Nd,s}}$) sources.

We estimate $\phi_{\mathrm{Nd,r}}$, $\phi_{\mathrm{Nd,d}}$, and $\phi_{\mathrm{Nd,h}}$ following the approach used by Dauphas *et al.* (2024) for iron. We assume that at steady-state, the Nd flux from rivers scales with the rate of continental chemical weathering, which itself is going to scale with the rate of CO_2 degassing through

$$\phi_{\mathrm{Nd,r}}(t) = r_{CO_2} r_{\phi_{\mathrm{mantle}}} \phi_{\mathrm{Nd,r}}(0), \qquad \text{(Eq. S-4)}$$

where $r_{CO_2} = 0.8$ is the Archean to present-day ratio of the fraction of CO_2 drawdown associated with continental weathering (Krissansen-Totton *et al.*, 2018), $r_{\phi_{\text{mantle}}} = 2.3$ is the Archean to present-day ratio of mantle heat flux (Patočka *et al.*, 2020), and $\phi_{\text{Nd,r}}(0) = 1.5 \times 10^9$ g/yr is the present-day global Nd river input flux (Xu *et al.*, 2023), resulting in $\phi_{\text{Nd,r}}(t) = 2.76 \times 10^9$ g/yr into the Archean oceans. The Nd river flux may have been affected by its speciation and pH-dependent adsorption on solid particles (Goldstein and Jacobsen, 1987), which is not accounted for here due to lack of constraints. The Archean to present-day ratio of mantle heat flux is also uncertain, as it could have been significantly lower than what we adopted here. Indeed, Korenaga (2008) argued that the mantle heat flux did not change much since 4 Ga.

For the flux of dust, we use the following scaling,

$$\phi_{\text{Nd,d}}(t) = r_A \cdot \phi_{\text{dust}}(0) \cdot r_{[Nd]_{EC}} \cdot [Nd]_d(0) \cdot f(t), \quad \text{(Eq. S-5)}$$

where $r_A = 0.5$ is the Archean to present-day ratio of areal extent of emerged continents (Korenaga *et al.*, 2017), $\phi_{\text{dust}}(0) = 440\ Tg/yr$ is the present-day dust input flux (Wu *et al.*, 2020), $r_{[Nd]_{EC}} = 0.65$ is the Archean to present-day ratio of Nd concentration of emerged continents (Ptáček *et al.*, 2020), $[Nd]_d(0) = 20\ \mu g/g$ is the present-day global mean Nd concentration in dust (Goldstein *et al.*, 1984), and $f(t) = 0.1$ is the Archean fraction of Nd in dust that dissolves along with Fe in seawater (Dauphas *et al.*, 2024; Greaves *et al.*, 1994), resulting in $\phi_{\text{Nd,d}}(t) = 2.86 \times 10^8$ g/yr during the Archean.

In the modern ocean, hydrothermal fluids represent a negligible source and in fact represent a net sink due to scavenging of Nd by particulate iron (German *et al.*, 1990). In the anoxic Archean ocean, high-temperature hydrothermal fluids could have released Fe and Nd into seawater without elemental fractionation (Jacobsen and Pimentel-Klose, 1988). We therefore use the following scaling,

$$\phi_{\text{Nd,h}}(t) = r_{\phi_{\text{hydro}}} \cdot \phi_{\text{hw}}(0) \cdot [Fe]_h(0) \cdot \left(\frac{Nd}{Fe}\right)_{\text{mafic}}(t), \quad \text{(Eq. S-6)}$$

where $r_{\phi_{\text{hydro}}} = 5$ is the maximum Archean to present-day ratio of hydrothermal heat flux (Lowell and Keller, 2003), $\phi_{\text{hw}}(0) = 5.9 \times 10^{16}$ g/yr is the present-day high-temperature hydrothermal water flux (Dauphas *et al.*, 2024), $[Fe]_h(0) = 5.8\ mmol/kg$ is the present-day Fe concentration in high-temperature hydrothermal fluid (Dauphas *et al.*,

2024), and $(Nd/Fe)_{\text{mafic}}(t) = 0.00013$ is the Nd/Fe ratio in Archean mafic rocks (Ptáček *et al.*, 2020), resulting in $\phi_{\text{Nd,h}}(t) = 1.25 \times 10^{10}$ g/yr during the Archean.

In the modern ocean, the flux from benthic sediments accounts for ~95% of total Nd sources (Rempfer *et al.*, 2011; Abbott *et al.*, 2015a, b; Haley *et al.*, 2017; Du *et al.*, 2020). The mechanisms of this benthic sediment Nd input are not yet defined, but the Nd flux seems to be dominated by deep-sea sediments (water depth > 3 km) and may be controlled by the extent of benthic seafloor area and sediment provenance, with no clear influence of the redox state of the sediments (Du *et al.*, 2018). We posit that in the Archean, the sediment source consistently scaled with the flux of other sources (Table S-1).

We make two different assumptions for that scaling: it could either represent 95% of the total flux including hydrothermal, or 95% of the total flux excluding hydrothermal. While the sediment source dominates the overall Nd flux, other sources play significant roles in the Nd cycle as they can influence the ε_{Nd} value of nearby water masses. Assuming that the benthic flux represents 95% of the total, we have $\phi_{\text{Nd}} = (\phi_{\text{Nd,r}} + \phi_{\text{Nd,d}} + \phi_{\text{Nd,h}})/5\% = 3.11 \times 10^{11}$ g/yr and $\phi_{\text{Nd,s}} = 95\%\phi_{\text{Nd}} = 2.95 \times 10^{11}$ g/yr. Assuming that the benthic flux represents 95% of the total excluding hydrothermal, we have $\phi_{\text{Nd,s}} = 5.79 \times 10^{10}$ g/yr and $\phi_{\text{Nd}} = \phi_{\text{Nd,r}} + \phi_{\text{Nd,d}} + \phi_{\text{Nd,h}} + \phi_{\text{Nd,s}} = 7.34 \times 10^{10}$ g/yr. In both cases, the benthic flux dominates all other fluxes (79% to 95% of the total).

For the first assumption, we use $[Nd]_{\text{sw}} = 1.43 \times 10^{-7}$ g/kg by taking the average of the Nd concentrations of 3.1-3.4 Ga seawater estimated from BIF magnetite of Badampahar greenstone belt (Ghosh and Baidya, 2017) and dolomite of Pilbara Block (Yamamoto *et al.*, 2004). For a 1.4×10^{21} kg ocean, this gives a total Nd inventory equal to 2.0×10^{14} g. The calculated Nd residence time in the Archean oceans is therefore $\tau_{\text{Nd}} = Nd/\phi_{\text{Nd}} = (2.0 \times 10^{14}\text{ g})/(3.11 \times 10^{11}\text{ g/yr}) = 643\ yr$. The Nd concentration in the Archean ocean is, however, poorly constrained, and we adopt a constant residence time of 643 yr in all simulations. Therefore, $[Nd]_{\text{sw}}$ becomes 3.37×10^{-8} g/kg for the second assumption.

In the modern ocean, Nd is removed from the water column by scavenging on particles following a first-order kinetic rate law $\phi_{\text{Nd,sink}} = k \cdot dt \cdot [Nd]_{sw}$, where $k = 1/\tau_{\text{Nd}}$ (Bacon and Anderson, 1982; Du *et al.*, 2020). We assume

that Nd removal in Precambrian oceans took place through the same mechanism with the same first-order kinetic law applying, and we set $k = 1/643\ yr^{-1}$ in our model to balance the input fluxes.

We estimate Archean $\varepsilon_{Nd,sw}$, $\varepsilon_{Nd,h}$, $\varepsilon_{Nd,r}$ and $\varepsilon_{Nd,d}$ values by taking the average ε_{Nd} of Superior-type BIFs compiled (Pongola BIF, Alexander *et al*., 2008; Marra Mamba BIF, Alibert and McCulloch, 1993; Benchmark BIF, Frei *et al*., 2008; Central Slave Cover Group BIF, Haugaard *et al*., 2016), depleted mantle-derived rocks (Vervoort and Blichert-Toft, 1999), and detrital sedimentary rocks (Garçon, 2021) respectively, assuming $\varepsilon_{Nd,r} = \varepsilon_{Nd,d}$ as river and dust Nd both reflect continental ε_{Nd}. Taking the average of ε_{Nd} of each rock type during the Archean (Fig. 3a), we have $\varepsilon_{Nd,sw} = +0.63$, $\varepsilon_{Nd,h} = +2.6$, and $\varepsilon_{Nd,r} = \varepsilon_{Nd,d} = -0.42$. We then solve for the benthic sediment isotopic composition $\varepsilon_{Nd,s}$ through a simple mass balance calculation that ensures that the source ε_{Nd} value is equal to seawater (the sink ε_{Nd} value is that of seawater),

$$\varepsilon_{Nd,sw} = \left(\varepsilon_{Nd,r} \times \phi_{Nd,r} + \varepsilon_{Nd,d} \times \phi_{Nd,d} + \varepsilon_{Nd,h} \times \phi_{Nd,h} + \varepsilon_{Nd,s} \times \phi_{Nd,s}\right)/\left(\phi_{Nd,r} + \phi_{Nd,d} + \phi_{Nd,h} + \phi_{Nd,s}\right). \quad \text{(Eq. S-7)}$$

By plugging in the values for Nd fluxes and isotopic compositions from above, we get $\varepsilon_{Nd,s} = +0.56$ for Scenario 1 and $\varepsilon_{Nd,s} = +0.26$ for Scenario 2.

We additionally consider a heterogeneous scenario (Scenario 3) where $\varepsilon_{Nd,s} = \varepsilon_{Nd,h}$ in sediments located closer to the hydrothermal source, and $\varepsilon_{Nd,s} = \varepsilon_{Nd,r}$ in sediments located closer to the continental sources. The magnitude of sediment flux carrying either isotopic signature is proportional to the magnitude of the corresponding flux.

Finally in Scenario 4, to account for the possible heterogeneity in ε_{Nd} values due to coexistence of juvenile and older crust in the late Archean, as is observed in detrital sediments of Archean age (Fig. 3a), we take the ε_{Nd} values of depleted mantle ($\varepsilon_{Nd,c,juv} = +3.4$) and continuous continental crust growth ($\varepsilon_{Nd,c,old} = -3.1$) models at ~2.5 to 3.0 Ga from Garçon (2021) as endmembers for rivers, aeolian dust, and benthic sediments $\varepsilon_{Nd,r}$, $\varepsilon_{Nd,d}$ and $\varepsilon_{Nd,s}$. Detrital sedimentary rocks indicate that this period saw an impulse of juvenile crust production from the depleted mantle (Garçon, 2021). We then solve for the relative contributions of these two endmember ε_{Nd} values into the Archean ocean such that the bulk $\varepsilon_{Nd,sw}$ is reproduced,

$$\varepsilon_{Nd,sw} = \frac{\left[\varepsilon_{Nd,c,old} \times x + \varepsilon_{Nd,c,juv} \times (1-x)\right]\left(\phi_{Nd,r} + \phi_{Nd,d} + \phi_{Nd,s}\right) + \varepsilon_{Nd,h} \times \phi_{Nd,h}}{\phi_{Nd,r} + \phi_{Nd,d} + \phi_{Nd,h} + \phi_{Nd,s}}, \quad \text{(Eq. S-8)}$$

yielding $x = 0.49$, meaning that meaning that 49% of the river, aeolian, and benthic sediment sources have enriched $\varepsilon_{Nd} = -3.1$ and the remaining 51% have depleted $\varepsilon_{Nd} = +3.4$. Such proportion of juvenile crust needed to explain the average BIF ε_{Nd} value is close to the value calculated by Garçon (2021) for the source of detrital sediments during this period (~50%).

The Nd riverine flux is applied in coastal grid cells around the supercontinents in the surface ocean, and the Nd dust flux is applied in all surface ocean grid cells. The Nd hydrothermal flux is applied along 'mid-ocean ridges' between 115°W and 125°W in the bottom ocean, and the Nd sediment flux is applied in all bottom ocean grid cells except those occupied by the hydrothermal flux. Nd sources are balanced by one sink, scavenging, which is parameterized following the first-order rate law discussed above, applied uniformly to all ocean cells.

To test our model's ability to reconstruct the source heterogeneity of ε_{Nd} as observed in the modern ocean and evaluate how sensitive it is to the sediment flux, we model ε_{Nd} in the modern ocean with and without a sediment flux (Fig. S-3). In the simulation aimed at reproducing the modern Nd cycle, we use modern river, dust and sediment Nd input fluxes and corresponding ε_{Nd} values that vary among basins based on Table 1 from Du *et al*. (2020). In the simulation aimed at evaluating the influence of the sediment flux, the global seawater ε_{Nd} is affected only by the river and dust fluxes. Despite variations in ε_{Nd} in the North Atlantic that contrast with observations due to reduced North Atlantic Deep Water formation in our modelled present-day ocean (Fig. S-4), incorporating a sediment Nd source with variable ε_{Nd} significantly improves the model's ability to capture the observed ε_{Nd} heterogeneity between Pacific and Atlantic Oceans, especially at depths >200 m, which is the bathymetry relevant for Precambrian BIF formation (Trendall, 2002).

Supplementary Figures

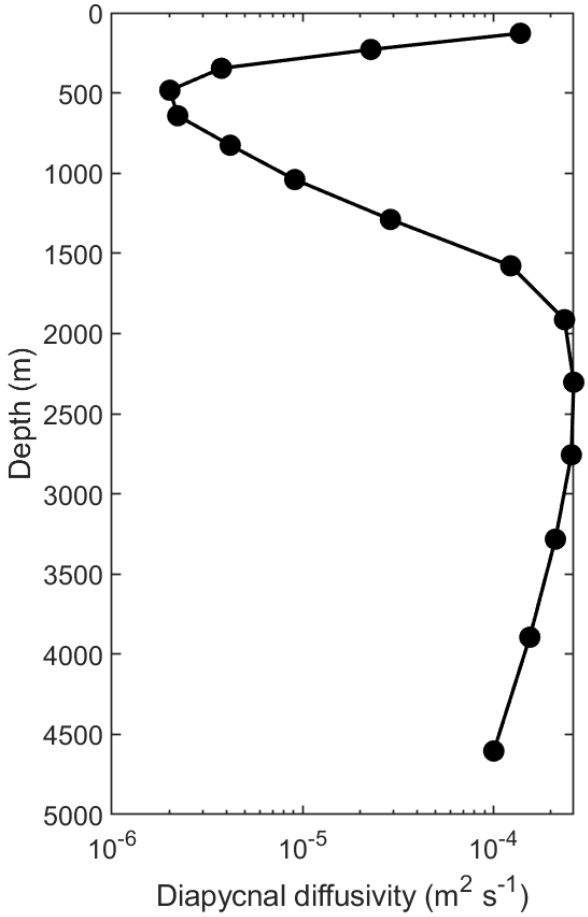

Figure S-1 Depth profile of diapycnal diffusivity in the present-day baseline model simulation. The profile shows the stratification-weighted horizontal average of the model's 3-dimensional diffusivity field.

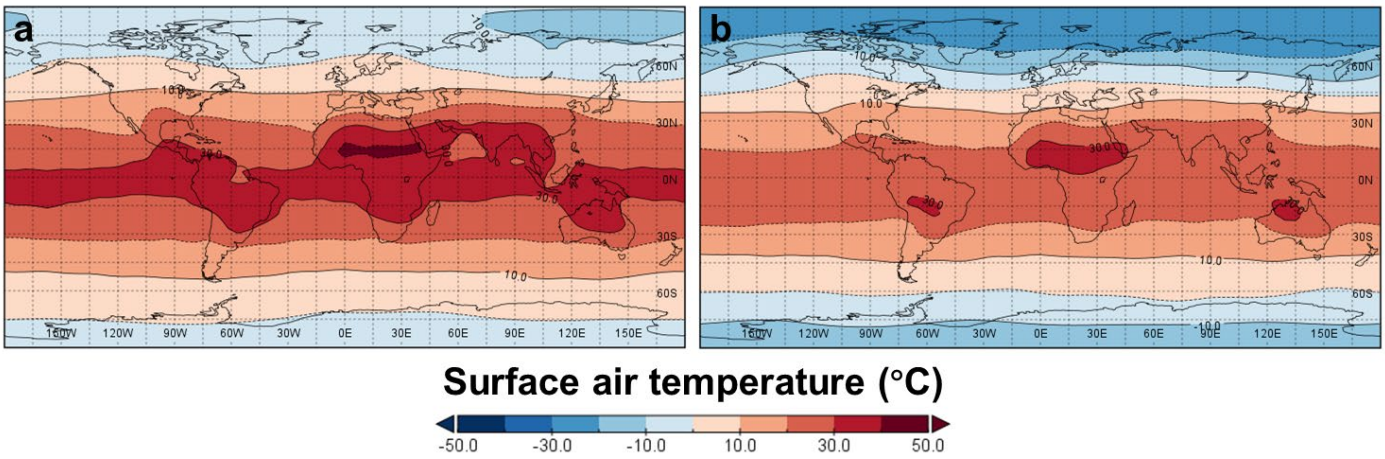

Figure S-2 Annual mean surface air temperature in (a) present-day baseline with ozone and (b) ozone-less baseline.

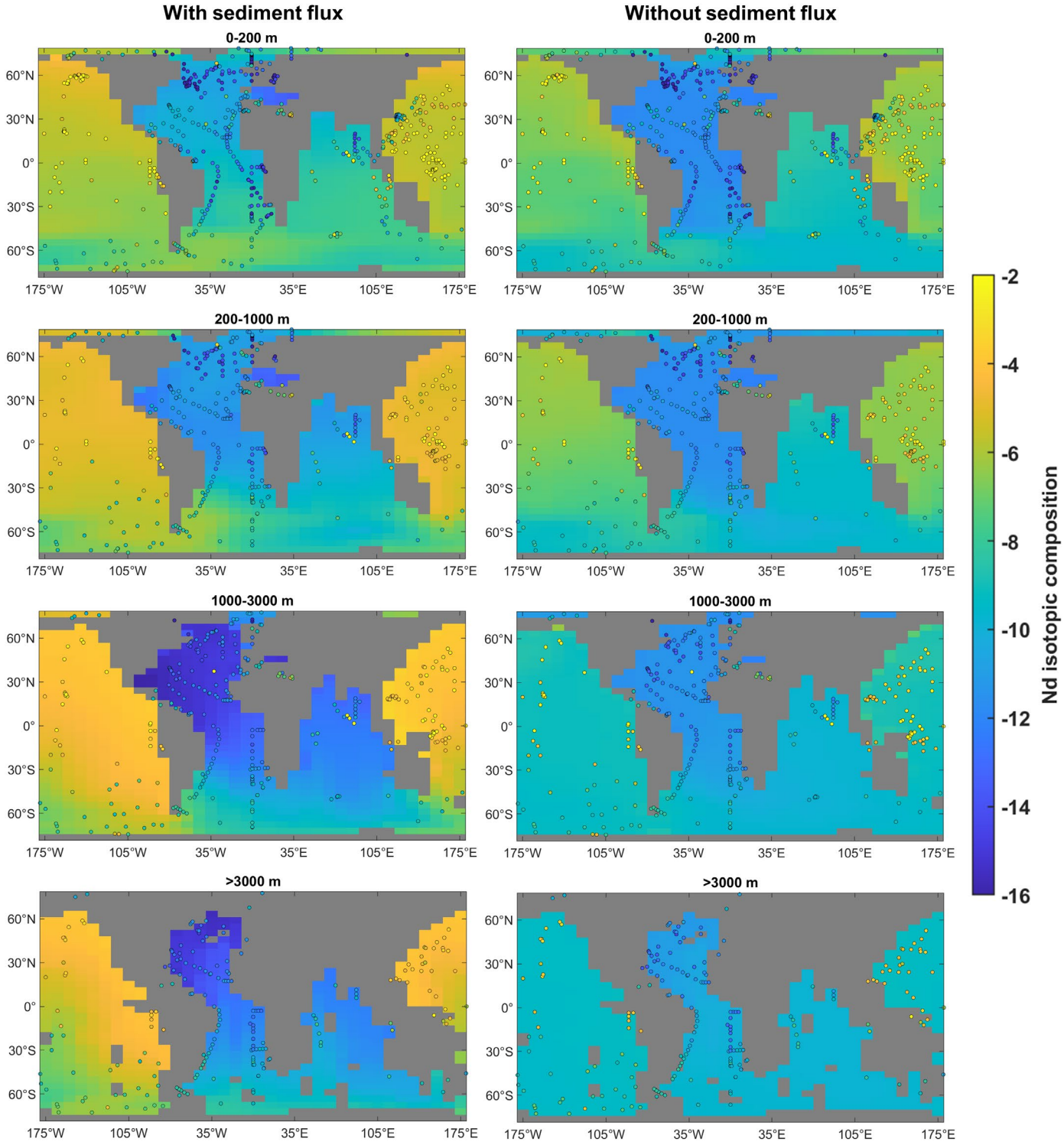

Figure S-3 Modelled Nd isotopic composition in present-day baseline with (left) or without (right) a benthic sediment source. Circles are observational data compiled by Robinson *et al.* (2023).

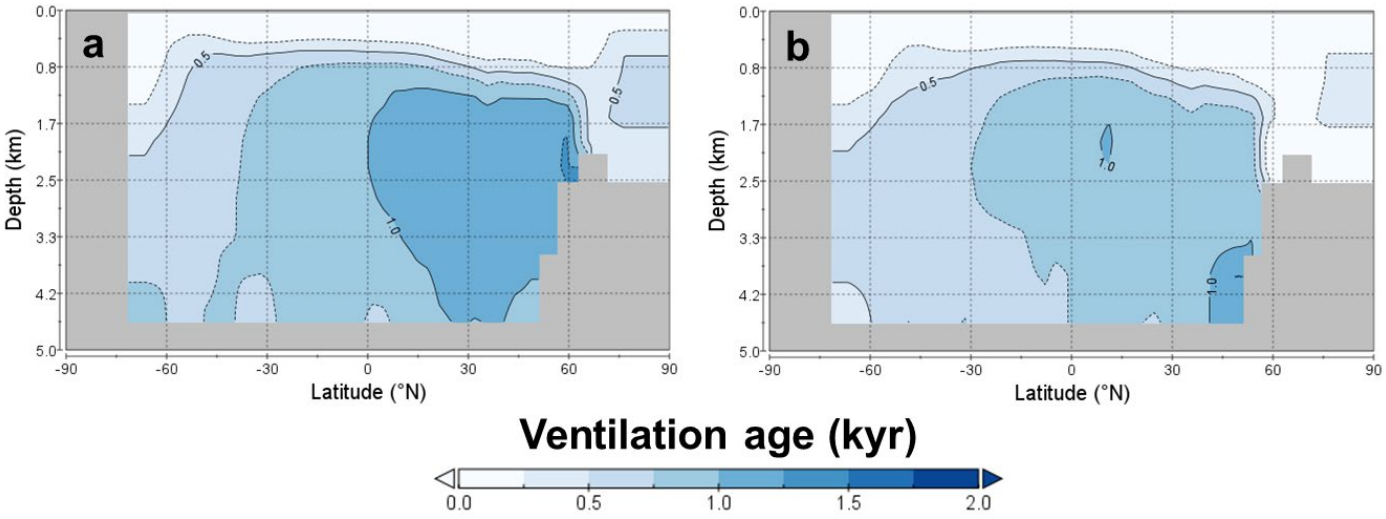

Figure S-4 Zonal mean water mass ventilation age in **(a)** present-day baseline with ozone and **(b)** ozone-less baseline.

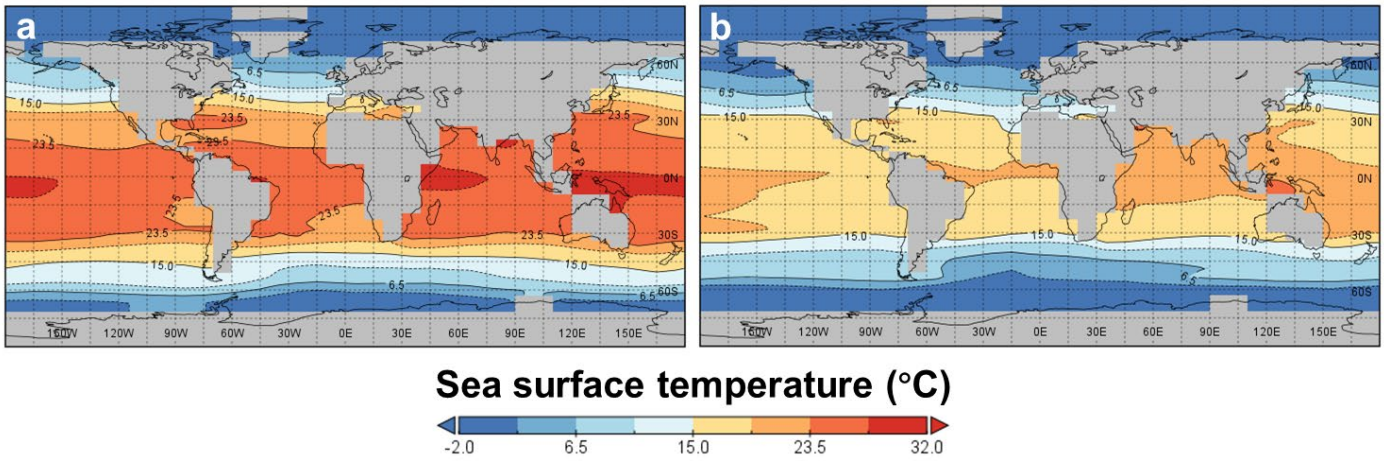

Figure S-5 Annual mean sea surface temperature in **(a)** present-day baseline with ozone and **(b)** ozone-less baseline.

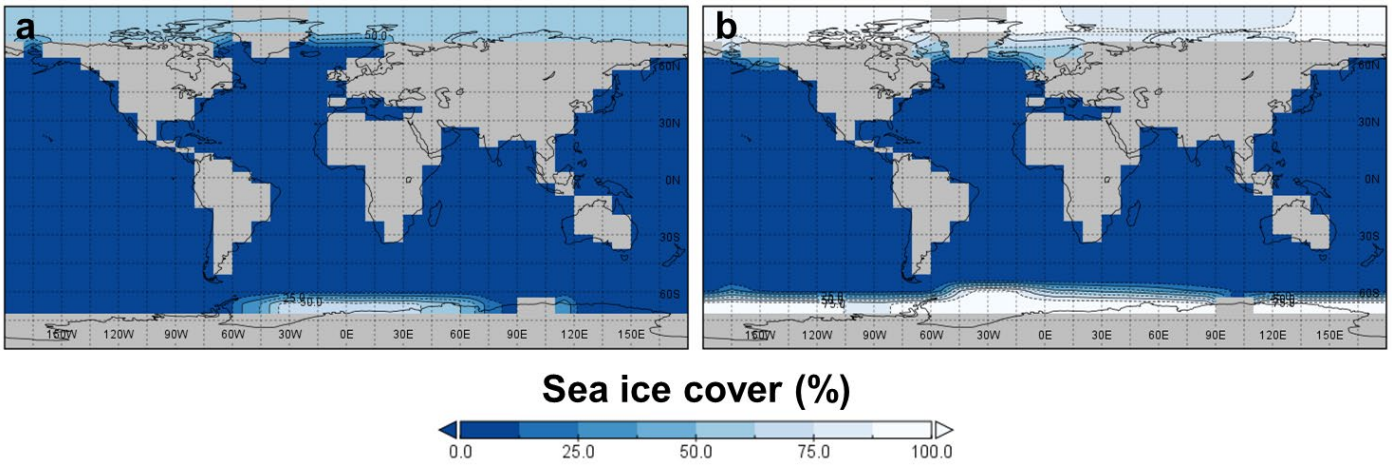

Figure S-6 Annual mean sea ice cover in **(a)** present-day baseline with ozone and **(b)** ozone-less baseline.

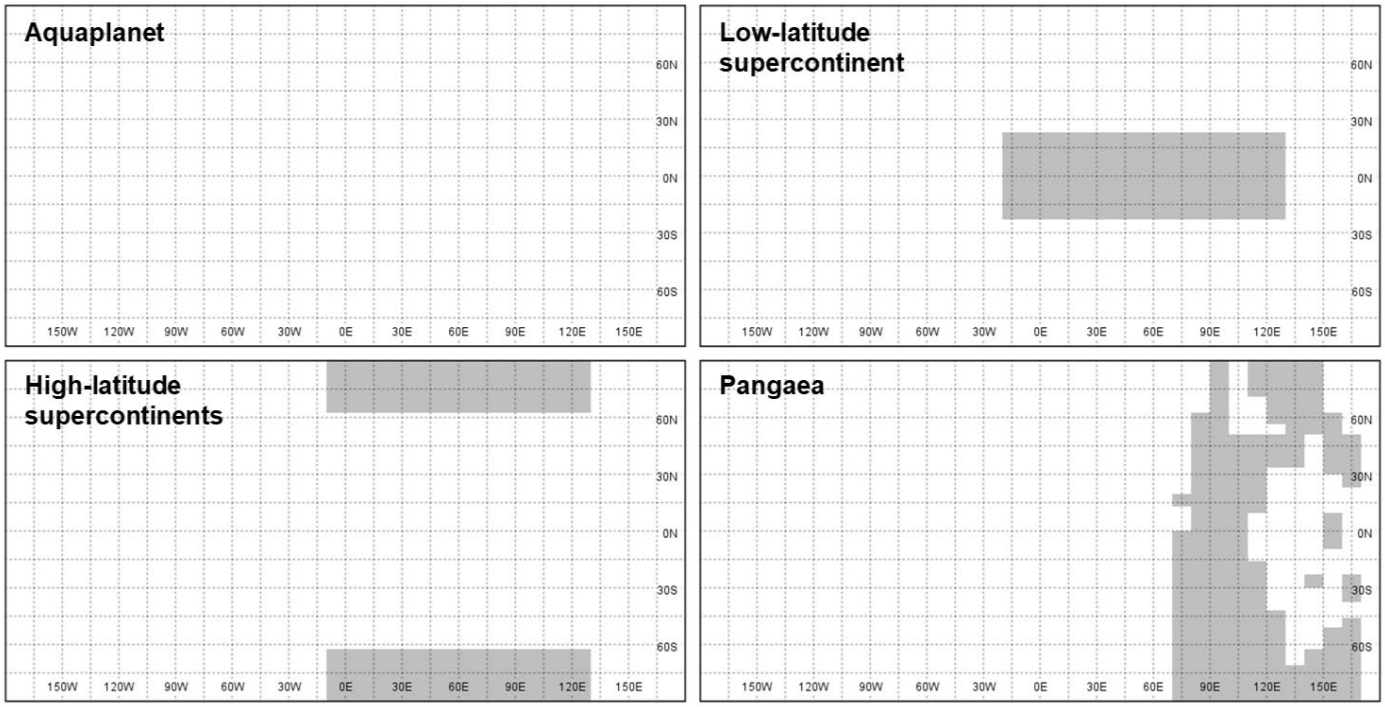

Figure S-7 Continental configurations used in sensitivity and historical simulations.

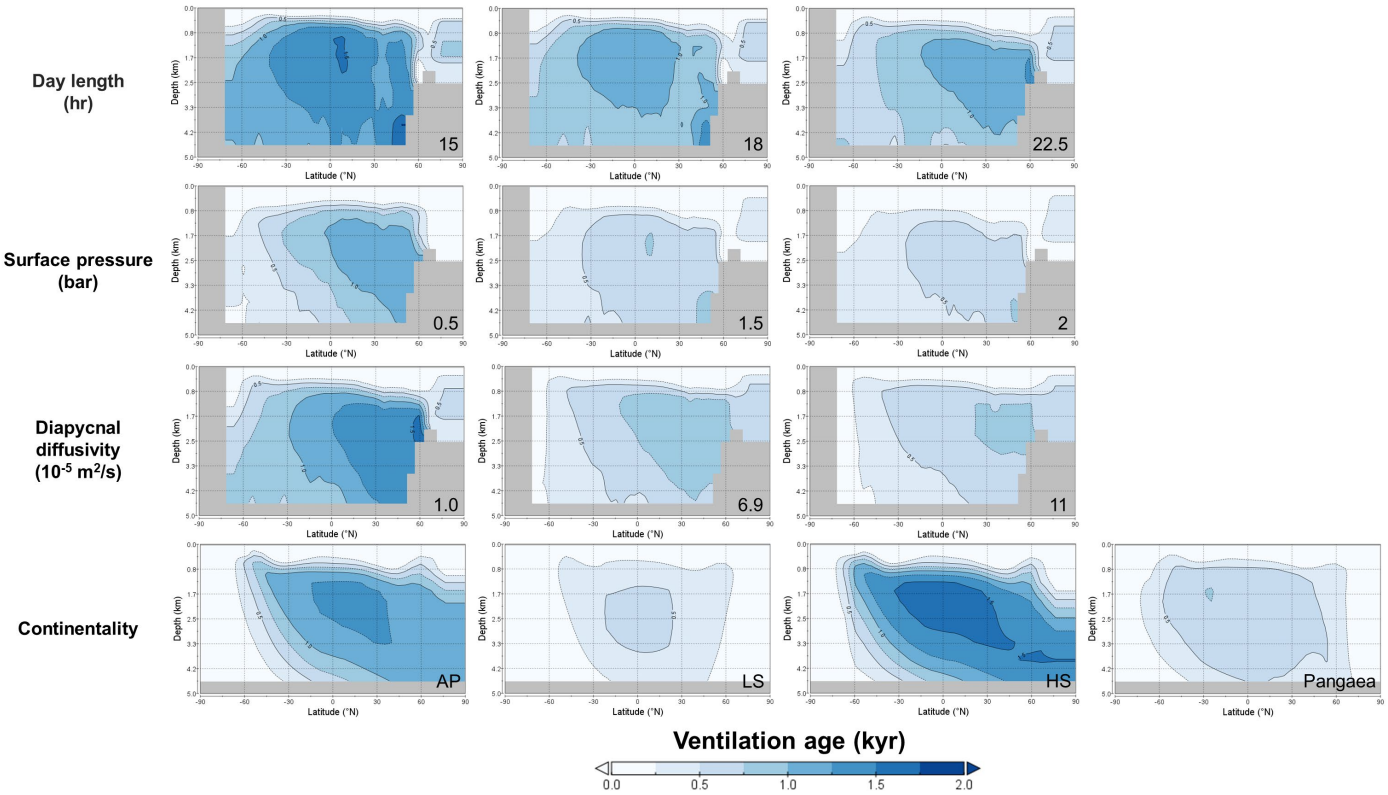

Figure S-8 Zonal mean water mass ventilation age in sensitivity tests. AP: aquaplanet; LS: low-latitude supercontinent; HS: high-latitude supercontinents.

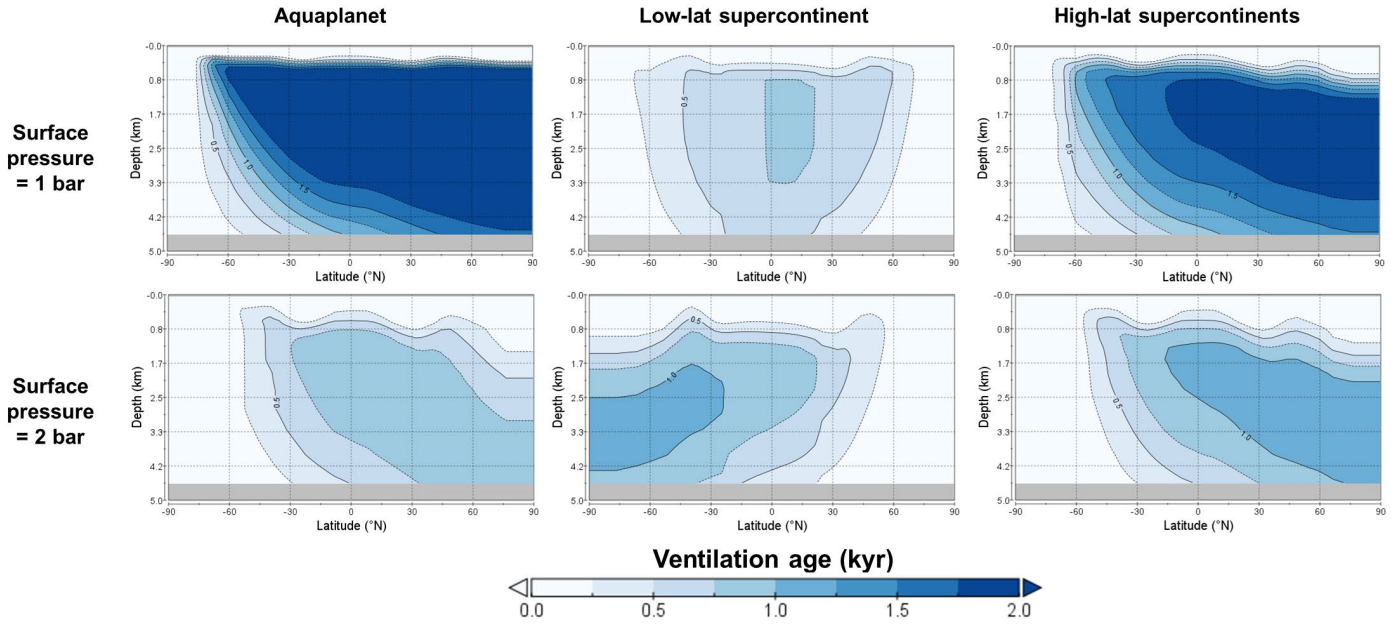

Figure S-9 Zonal mean water mass ventilation age in 'Paleoarchean' simulations with day length = 15 hr and individual diapycnal diffusivities (see Table 1 for details). Note that the color bar is saturated in the top left panel, where the maximum age is 2.4 kyr.

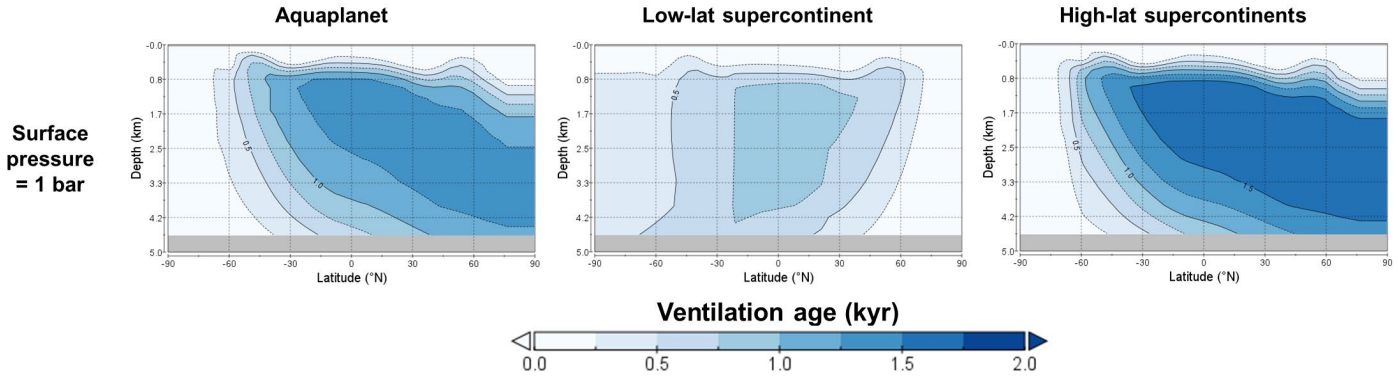

Figure S-10 Zonal mean water mass ventilation age in 'Neoarchean' simulations with day length = 18 hr and individual diapycnal diffusivities (see Table 1 for details).

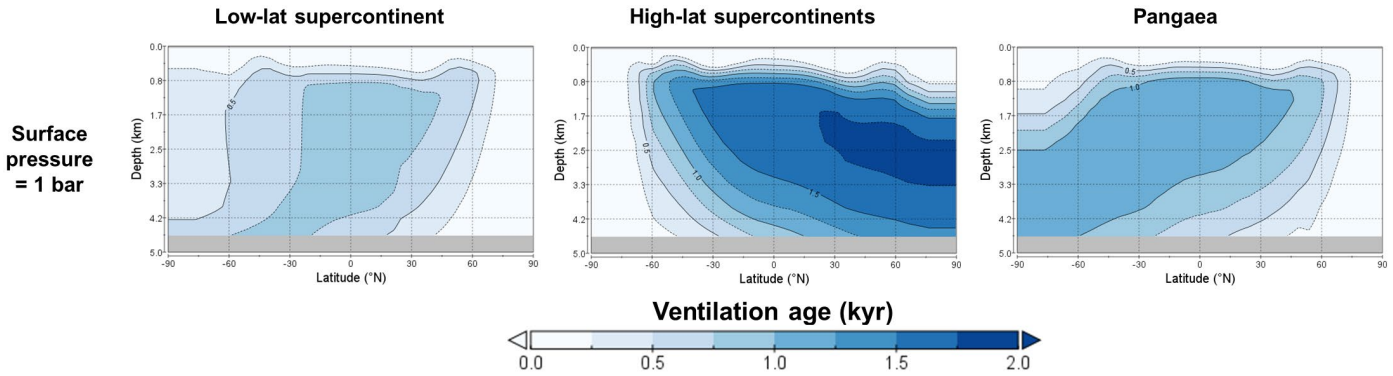

Figure S-11 Zonal mean water mass ventilation age in 'Paleoproterozoic' simulations with day length = 18 hr and individual diapycnal diffusivities (see Table 1 for details).

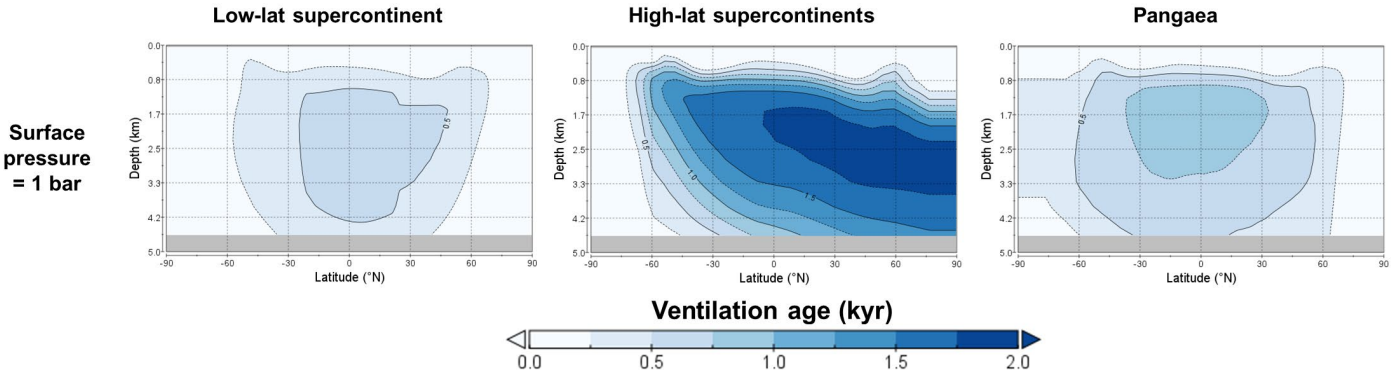

Figure S-12 Zonal mean water mass ventilation age in 'Meso/Neoproterozoic' simulations with day length = 22.5 hr and individual diapycnal diffusivities (see Table 1 for details).

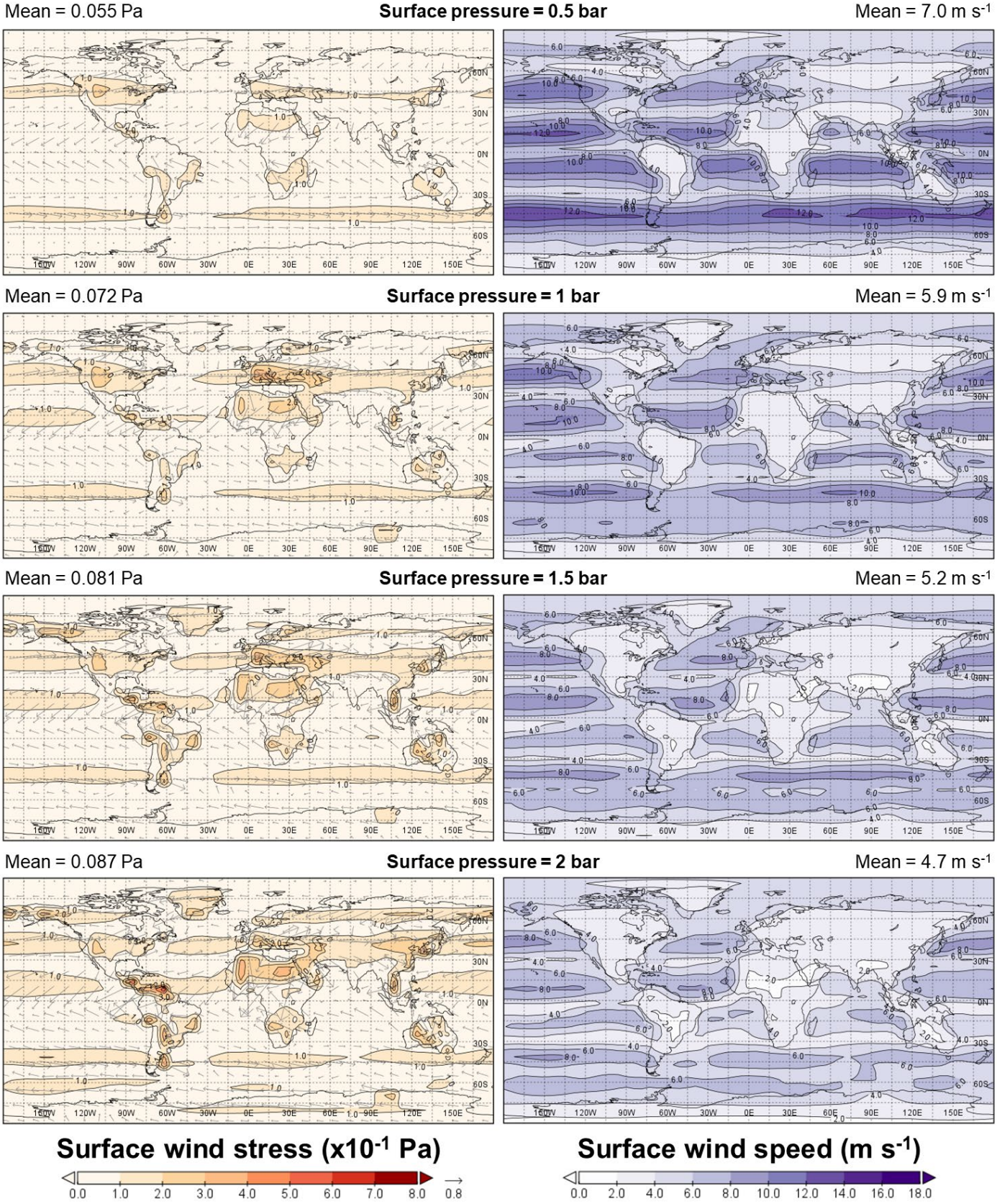

Figure S-13 Annual mean surface wind stress and speed in ozone-less baseline *vs*. surface pressure sensitivity tests.

Supplementary Information References

Table S-1 compiles the parameter values used in the modelling the Nd cycle during the Archean.

	Scenario 1	Scenario 2	Scenario 3		Scenario 4	
Seawater [Nd] (g/kg)	1.43×10^{-7}	3.37×10^{-8}	Same as Scenario 1		Same as Scenario 2	
Seawater ε_{Nd}	+0.63	Same as Scenario 1			Same as Scenario 1	
Hydrothermal Nd source (g/yr)	1.25×10^{10}					
Hydrothermal flux ε_{Nd}	+2.6					
Riverine Nd source (g/yr)	2.76×10^{9}				1.35×10^{9}	1.41×10^{9}
Riverine flux ε_{Nd}	-0.42				-3.1	+3.4
Dust Nd source (g/yr)	2.86×10^{8}				1.40×10^{8}	1.46×10^{8}
Dust flux ε_{Nd}	-0.42				-3.1	+3.4
Sediment Nd source (g/yr)	2.95×10^{11}	5.79×10^{10}	2.00×10^{11}	9.50×10^{10}	2.83×10^{10}	2.96×10^{10}
Sediment flux ε_{Nd}	+0.56	+0.26	-0.42	+2.6	-3.1	+3.4

Supplementary Information References

Abbott, A.N., Haley, B.A., McManus, J. (2015a) Bottoms up: Sedimentary control of the deep North Pacific Ocean's εNd signature. *Geology* 43, 1035-1035. https://doi.org/10.1130/G37114.1

Abbott, A.N., Haley, B.A., McManus, J., Reimers, C.E. (2015b) The sedimentary flux of dissolved rare earth elements to the ocean. *Geochimica et Cosmochimica Acta* 154, 186-200. https://doi.org/10.1016/j.gca.2015.01.010

Alexander, B.W., Bau, M., Andersson, P., Dulski, P. (2008) Continentally-derived solutes in shallow Archean seawater: rare earth element and Nd isotope evidence in iron formation from the 2.9 Ga Pongola Supergroup, South Africa. *Geochimica et Cosmochimica Acta* 72, 378-394. https://doi.org/10.1016/j.gca.2007.10.028

Alibert, C., McCulloch, M.T. (1993) Rare earth element and neodymium isotopic compositions of the banded iron-formations and associated shales from Hamersley, Western Australia. *Geochimica et Cosmochimica Acta* 57, 187-204. https://doi.org/10.1016/0016-7037(93)90478-F

Bacon, M.P., Anderson, R.F. (1982) Distribution of thorium isotopes between dissolved and particulate forms in the deep sea. *Journal of Geophysical Research: Oceans* 87, 2045-2056. https://doi.org/10.1029/JC087iC03p02045

Crichton, K.A., Ridgwell, A., Lunt, D.J., Farnsworth, A., Pearson, P.N. (2021) Data-constrained assessment of ocean circulation changes since the middle Miocene in an Earth system model. *Climate of the Past* 17, 2223-2254. https://doi.org/10.5194/cp-17-2223-2021

Dauphas, N., Heard, A.W., Rego, E.S., Rouxel, O., Marin-Carbonne, J., Pasquier, V., Bekker, A., Rowley, D.B., (2024) Past and present dynamics of the iron biogeochemical cycle. *Reference Module in Earth Systems and Environmental Sciences*. https://doi.org/10.1016/B978-0-323-99762-1.00059-0

Davies, H.S., Green, J.A.M., Duarte, J.C. (2020) Back to the future II: tidal evolution of four supercontinent scenarios. *Earth System Dynamics* 11, 291–299. https://doi.org/10.5194/esd-11-291-2020

Du, J., Haley, B.A., Mix, A.C., Walczak, M.H., Praetorius, S.K. (2018) Flushing of the deep Pacific Ocean and the deglacial rise of atmospheric CO2 concentrations. *Nature Geoscience* 11, 749-755. https://doi.org/10.1038/s41561-018-0205-6

Du, J., Haley, B.A., Mix, A.C. (2020) Evolution of the Global Overturning Circulation since the Last Glacial Maximum based on marine authigenic neodymium isotopes. *Quaternary Science Reviews* 241, 106396. https://doi.org/10.1016/j.quascirev.2020.106396

Fraedrich, K., Jansen, H., Kirk, E., Luksch, U., Lunkeit, F. (2005) The Planet Simulator: Towards a user friendly model. *Meteorologische Zeitschrift* 14, 299-304. https://doi.org/10.1127/0941-2948/2005/0043

Frei, R., Dahl, P.S., Duke, E.F., Frei, K.M., Hansen, T.R., Frandsson, M.M., Jensen, L.A. (2008) Trace element and isotopic characterization of Neoarchean and Paleoproterozoic iron formations in the Black Hills (South Dakota, USA): assessment of chemical change during 2.9–1.9 Ga deposition bracketing the 2.4–2.2 Ga first rise of atmospheric oxygen. *Precambrian Research* 162, 441-474. https://doi.org/10.1016/j.precamres.2007.10.005

Garçon, M. (2021) Episodic growth of felsic continents in the past 3.7 Ga. *Science advances* 7, eabj1807. DOI: 10.1126/sciadv.abj1807

German, C.R., Klinkhammer, G.P., Edmond, J.M., Mura, A., Elderfield, H. (1990) Hydrothermal scavenging of rare-earth elements in the ocean. *Nature* 345, 516-518. https://doi.org/10.1038/345516a0

Ghosh, R., Baidya, T.K. (2017) Using BIF magnetite of the Badampahar greenstone belt, Iron Ore Group, East Indian Shield to reconstruct the water chemistry of a 3.3–3.1 Ga sea during iron oxyhydroxides precipitation. *Precambrian Research* 301, 102-112. https://doi.org/10.1016/j.precamres.2017.09.006

Goldstein, S.J., Jacobsen, S.B. (1987) The Nd and Sr isotopic systematics of river-water dissolved material: Implications for the sources of Nd and Sr in seawater. *Chemical Geology: Isotope Geoscience section* 66, 245-272. https://doi.org/10.1016/0168-9622(87)90045-5

Goldstein, S.L., O'nions, R.K., Hamilton, P.J. (1984) A Sm-Nd isotopic study of atmospheric dusts and particulates from major river systems. *Earth and Planetary Science letters* 70, 221-236. https://doi.org/10.1016/0012-821X(84)90007-4

Greaves, M.J., Statham, P.J., Elderfield, H. (1994) Rare earth element mobilization from marine atmospheric dust into seawater. *Marine Chemistry* 46, 255-260. https://doi.org/10.1016/0304-4203(94)90081-7

Haley, B.A., Du, J., Abbott, A.N., McManus, J. (2017) The impact of benthic processes on rare earth element and neodymium isotope distributions in the oceans. *Frontiers in Marine Science* 4, 426. https://doi.org/10.3389/fmars.2017.00426

Haugaard, R., Ootes, L., Creaser, R.A., Konhauser, K.O. (2016) The nature of Mesoarchaean seawater and continental weathering in 2.85 Ga banded iron formation, Slave craton, NW Canada. *Geochimica et Cosmochimica Acta* 194, 34-56. https://doi.org/10.1016/j.gca.2016.08.020

Jacobsen, S.B., Pimentel-Klose, M.R. (1988) A Nd isotopic study of the Hamersley and Michipicoten banded iron formations: the source of REE and Fe in Archean oceans. *Earth and Planetary Science Letters* 87, 29-44. https://doi.org/10.1016/0012-821X(88)90062-3

Korenaga, J. (2008) Urey ratio and the structure and evolution of Earth's mantle. *Reviews of Geophysics* 46, RG2007. https://doi.org/10.1029/2007RG000241

Korenaga, J., Planavsky, N.J., Evans, D.A. (2017) Global water cycle and the coevolution of the Earth's interior and surface environment. *Philosophical Transactions of the Royal Society A: Mathematical, Physical and Engineering Sciences* 375, 20150393. https://doi.org/10.1098/rsta.2015.0393

Krissansen-Totton, J., Arney, G.N., Catling, D.C. (2018) Constraining the climate and ocean pH of the early Earth with a geological carbon cycle model. *Proceedings of the National Academy of Sciences* 115, 4105-4110. https://doi.org/10.1073/pnas.1721296115

Kunze, E., Firing, E., Hummon, J.M., Chereskin, T.K., Thurnherr, A.M. (2006) Global Abyssal Mixing Inferred from Lowered ADCP Shear and CTD Strain Profiles. *Journal of Physical Oceanography* 36, 1553–1576. https://doi.org/10.1175/JPO2926.1

Lowell, R.P., Keller, S.M. (2003) High-temperature seafloor hydrothermal circulation over geologic time and Archean banded iron formations. *Geophysical Research Letters* 30, 1391. https://doi.org/10.1029/2002GL016536

Oliver, K.I.C., Edwards, N.R. (2008) Location of potential energy sources and the export of dense water from the Atlantic Ocean. *Geophysical Research Letters* 35, L22604. https://doi.org/10.1029/2008GL035537

Paradise, A., Fan, B.L., Menou, K., Lee, C. (2021) Climate diversity in the solar-like habitable zone due to varying background gas pressure. *Icarus* 358, 114301. https://doi.org/10.1016/j.icarus.2020.114301

Paradise, A., Macdonald, E., Menou, K., Lee, C., Fan, B.L. (2022) ExoPlaSim: Extending the Planet Simulator for exoplanets. *Monthly Notices of the Royal Astronomical Society* 511, 3272-3303. https://doi.org/10.1093/mnras/stac172

Patočka, V., Šrámek, O., Tosi, N. (2020) Minimum heat flow from the core and thermal evolution of the Earth. *Physics of the Earth and Planetary Interiors* 305, 106457. https://doi.org/10.1016/j.pepi.2020.106457

Ptáček, M.P., Dauphas, N., Greber, N.D. (2020) Chemical evolution of the continental crust from a data-driven inversion of terrigenous sediment compositions. *Earth and Planetary Science Letters* 539, 116090. https://doi.org/10.1016/j.epsl.2020.116090

Rempfer, J., Stocker, T.F., Joos, F., Dutay, J.C., Siddall, M. (2011) Modelling Nd-isotopes with a coarse resolution ocean circulation model: Sensitivities to model parameters and source/sink distributions. *Geochimica et Cosmochimica Acta* 75, 5927-5950. https://doi.org/10.1016/j.gca.2011.07.044

Ridgwell, A. (2017) The Bumper Book of muffins (The cGENIE.muffin user-manual and introduction to Earth system modelling). https://www.seao2.info/cgenie/docs/muffin.pdf

Robinson, S., Ivanovic, R.F., Gregoire, L.J., Tindall, J., van de Flierdt, T., *et al.* (2023) Simulating marine neodymium isotope distributions using Nd v1. 0 coupled to the ocean component of the FAMOUS–MOSES1 climate model: sensitivities to reversible scavenging efficiency and benthic source distributions. *Geoscientific Model Development* 16, 1231-1264. https://doi.org/10.5194/gmd-16-1231-2023

Trendall, A.F. (2002) The significance of iron-formation in the Precambrian stratigraphic record. *Precambrian sedimentary environments: A modern approach to ancient depositional systems*, 33-66. https://doi.org/10.1002/9781444304312.ch3

Vervoort, J.D., Blichert-Toft, J. (1999) Evolution of the depleted mantle: Hf isotope evidence from juvenile rocks through time. *Geochimica et Cosmochimica Acta* 63, 533-556. https://doi.org/10.1016/S0016-7037(98)00274-9

Waterhouse, A.F., Mackinnon, J.A., Nash, J.D., Alford, M.H., Kunze, E., *et al.* (2014) Global Patterns of Diapycnal Mixing from Measurements of the Turbulent Dissipation Rate. *Journal of Physical Oceanography* 44, 1854–1872. https://doi.org/10.1175/JPO-D-13-0104.1

Webb, D.J. (1982) Tides and the evolution of the Earth-Moon system. *Geophysical Journal International* 70, 261–271. https://academic.oup.com/gji/article-abstract/70/1/261/708791

Wu, C., Lin, Z., Liu, X. (2020) The global dust cycle and uncertainty in CMIP5 (Coupled Model Intercomparison Project phase 5) models. *Atmospheric Chemistry and Physics* 20, 10401-10425. https://doi.org/10.5194/acp-20-10401-2020

Xu, A., Hathorne, E., Laukert, G., Frank, M. (2023) Overlooked riverine contributions of dissolved neodymium and hafnium to the Amazon estuary and oceans. *Nature Communications* 14, 4156. https://doi.org/10.1038/s41467-023-39922-3

Yamamoto, K., Itoh, N., Matsumoto, T., Tanaka, T., Adachi, M. (2004) Geochemistry of Precambrian carbonate intercalated in pillows and its host basalt: implications for the REE composition of circa 3.4 Ga seawater. *Precambrian Research* 135, 331-344. https://doi.org/10.1016/j.precamres.2004.09.006

Yang, J., Jansen, M.F., Macdonald, F.A., Abbot, D.S. (2017) Persistence of a freshwater surface ocean after a snowball Earth. *Geology* 45, 615–618. https://doi.org/10.1130/G38920.1